HHS Public Access

Author manuscript

Cell Rep. Author manuscript; available in PMC 2020 February 08.

Published in final edited form as:

Cell Rep. 2019 October 29; 29(5): 1274–1286.e6. doi:10.1016/j.celrep.2019.09.063.

Dysregulation of Mitochondrial Ca^{2+} Uptake and Sarcolemma Repair Underlie Muscle Weakness and Wasting in Patients and Mice Lacking MICU1

Valentina Debattisti[1], **Adam Horn**[2,3], **Raghavendra Singh**[1], **Erin L. Seifert**[1], **Marshall W. Hogarth**[2,3], **Davi A. Mazala**[2,3], **Kai Ting Huang**[1], **Rita Horvath**[4,5], **Jyoti K. Jaiswal**[2,3,*], **György Hajnóczky**[1,6,*]

[1]MitoCare Center for Mitochondrial Imaging Research and Diagnostics, Department of Pathology, Anatomy and Cell Biology, Thomas Jefferson University, Philadelphia, PA, USA

[2]Center for Genetic Medicine Research, Children's National Health System, 111 Michigan Avenue Northwest, Washington, DC 20010, USA

[3]Department of Genomics and Precision Medicine, George Washington University School of Medicine and Health Sciences, Washington, DC 20052, USA

[4]Wellcome Centre for Mitochondrial Research, Institute of Genetic Medicine, Newcastle University, Newcastle upon Tyne, UK

[5]Present address: Department of Clinical Neurosciences, University of Cambridge, Cambridge, UK

[6]Lead Contact

SUMMARY

Muscle function is regulated by Ca^{2+}, which mediates excitation-contraction coupling, energy metabolism, adaptation to exercise, and sarcolemmal repair. Several of these actions rely on Ca^{2+} delivery to the mitochondrial matrix via the mitochondrial Ca^{2+} uniporter, the pore of which is formed by mitochondrial calcium uniporter (MCU). MCU's gatekeeping and cooperative activation are controlled by MICU1. Loss-of-protein mutation in MICU1 causes a neuromuscular disease. To determine the mechanisms underlying the muscle impairments, we used MICU1 patient cells and skeletal muscle-specific MICU1 knockout mice. Both these models show a lower threshold for MCU-mediated Ca^{2+} uptake. Lack of MICU1 is associated with impaired mitochondrial Ca^{2+} uptake during excitation-contraction, aerobic metabolism impairment, muscle weakness, fatigue, and myofiber damage during physical activity. MICU1 deficit compromises

*Correspondence: jkjaiswal@cnmc.org (J.K.J.), gyorgy.hajnoczky@jefferson.edu (G.H.).

AUTHOR CONTRIBUTIONS

Conceptualization, V.D., G.H., A.H., J.K.J., and E.L.S.; Investigation, V.D., A.H., M.W.H., R.H., D.A.M., R.S., and K.T.H.; Writing, V.D., G.H., A.H., J.K.J., and E.L.S.; Funding Acquisition, G.H. and J.K.J.

SUPPLEMENTAL INFORMATION

Supplemental Information can be found online at https://doi.org/10.1016/j.celrep.2019.09.063.

DECLARATION OF INTERESTS

The authors declare no competing interests.

mitochondrial Ca^{2+} uptake during sarcolemmal injury, which causes ineffective repair of the damaged myofibers. Thus, dysregulation of mitochondrial Ca^{2+} uptake hampers myofiber contractile function, likely through energy metabolism and membrane repair.

Graphical Abstract

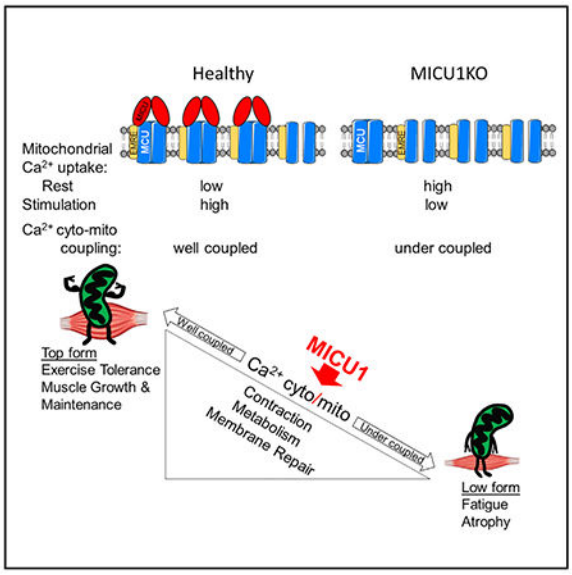

In Brief

Debattisti et al. report that skeletal muscle-specific loss of mitochondrial Ca^{2+} uptake 1 (MICU1) in mouse impairs mitochondrial calcium signaling, energy metabolism, and membrane repair, leading to muscle weakness, fatigue, myofiber damage, and high CK levels, recapitulating the muscle symptoms of MICU1 loss in patients.

INTRODUCTION

Skeletal muscle (SM) Ca^{2+} homeostasis is crucial for both excitation-contraction (EC) coupling and relaxation. When an action potential depolarizes the sarcolemmal membrane, L-type Ca^{2+} channels are activated and trigger the release of Ca^{2+} from the “calcium release units” (CRUs) of the sarcoplasmic reticulum (SR) (Franzini-Armstrong, 2018; Hernández-Ochoa et al., 2016). Ca^{2+} released from SR through the ryanodine receptor (RyR) Ca^{2+} channels binds to troponin, which undergoes a conformational change and pulls tropomyosin away from the actin active site allowing cross-bridge formation between actin and myosin and therefore provoking muscle contraction. Conversely, to allow relaxation, Ca^{2+} is pumped back into the SR, troponin loses its Ca^{2+}, and tropomyosin reverts to its off position. To match the energy requirements for contraction, mitochondria adjacent to CRUs take up Ca^{2+}, which in turn stimulates the Krebs cycle and ATP production (Eisner et al., 2013; Jouaville et al., 1999). SM-derived mitoplasts (representing the inner mitochondrial membrane [IMM]) display a much greater Ca^{2+} current density than other tissues like liver, kidney, and heart (Fieni et al., 2012), suggesting a pivotal role for mitochondrial Ca^{2+} uptake, specifically in SM function. Nevertheless, the full extent of the role of mitochondrial

Ca^{2+} uptake in SM function and disease remains elusive, in part because the molecular identity of the mitochondrial Ca^{2+} uniporter (mtCU) complex has been only recently determined (Baughman et al., 2011; De Stefani et al., 2011; Plovanich et al., 2013; Raffaello et al., 2013; Sancak et al., 2013).

The first animal model for mitochondrial calcium uniporter (MCU) deficiency, the pore component of the mtCU complex, a whole body MCU knockout ($MCU^{-/-}$), showed impairment in exercise capacity and muscle strength (Pan et al., 2013). However, when the ablation of MCU was achieved in a different genetic mouse background, MCU loss was embryonic lethal (Murphy et al., 2014). This suggests that mitochondrial Ca^{2+} uptake is central to life, and compensatory mechanisms could explain the discordant phenotypes retrieved in the different $MCU^{-/-}$ models. Very recently, two studies linked striated muscle-specific deletion of MCU to decreased acute exercise and increased fatty acid utilization, supporting a role of mitochondrial Ca^{2+} uptake in contractile function via oxidative metabolism (Gherardi etal., 2019; Kwong etal., 2018). Genetic manipulation of MCU expression has also been shown to affect the SM trophic response in mice (Mammucari et al., 2015), while in human subjects physical exercise has been demonstrated to cause increased protein levels of MCU (Zampieri et al., 2016). To our knowledge, no pathogenic human MCU mutations have been described yet, whereas pathogenic mutations in the mtCU regulatory subunits MICU1 and MICU2 have been described (Lewis-Smith et al., 2016; Logan et al., 2014; Musa et al., 2019; Shamseldin et al., 2017), shifting the focus to the MCU regulating subunits of the mtCU as potential players in pathophysiology. The Ca^{2+}-sensing protein MICU1 has been characterized as responsible for gatekeeping and cooperative activation of MCU (Csordás et al., 2013; Mallilankaraman et al., 2012; Perocchi et al., 2010; Wang et al., 2014), together with its isoform and potential interacting partner MICU2 (Kamer and Mootha, 2014; Patron et al., 2014; Plovanich et al., 2013). MICU1 is required for extrauterine life and for liver regeneration in mice as its loss leads to sensitization Ca^{2+} overload-induced mitochondrial permeability transition pore (PTP) opening in hepatocytes (Antony et al., 2016). MICU1 is particularly interesting in SM, where the function is tightly dependent on mitochondrial Ca^{2+} and the cells express a specific splicing variant of the protein that confers to SM mitochondria high responsiveness to sarcoplasmic Ca^{2+} signals (Vecellio Reane et al., 2016).

With the above studies suggesting a specific and important role of mtCU in SM function, it is not surprising that abnormal Ca^{2+} handling results in SM dysfunction and disease with mitochondrial involvement. Mutations in the RyR1, which are associated with congenital central core myopathy result in enhanced SR Ca^{2+} leak, which leads to progressive mitochondrial damage and decreased ability to generate force (Boncompagni et al., 2009; Durham et al., 2008; Yang et al., 2003). Abnormal mitochondrial Ca^{2+} handling has also been implicated in the pathogenesis of Ullrich congenital muscular dystrophy (UCMD) and Bethlem myopathy (BM), characterized by an increased sensitivity to PTP opening (Angelin et al., 2008; Tiepolo et al., 2009), leading to activation of a mitochondrial death pathway. Mutations of MICU1 have been linked to a neuronal and muscular disorder in humans (Lewis-Smith et al., 2016; Logan et al., 2014). The patients present with proximal muscle weakness and episodes of fatigue and lethargy, develop muscle aches after exercise, and during these attacks have elevated levels of creatine kinase (CK) activity, which is indicative

of cell damage due to the physical stress. Pathological mutations have been described also for the MICU1 paralog, MICU2. Patients with mutated MICU2 show encephalopathy with severe cognitive impairment without a sign of myopathy (Shamseldin et al., 2017). Thus, lack of MICU1 seems to be of greater consequence for normal SM physiology.

A common mechanism of SM degeneration is deficiency in the mechanism of repair of the sarcolemmal membrane, as already reported for mouse models for limb girdle muscular dystrophy 2B (Bansal et al., 2003; Cooper and Head, 2015; Defour et al., 2014b; McGreevy et al., 2015). Membrane repair defects have been recently linked to lack of MCU, highlighting the importance of a role for mitochondrial Ca^{2+} uptake in sarcolemma repair (Horn et al., 2017). In the mouse model of the lethal muscle disease Duchenne muscular dystrophy, dysregulation of calcium and mitochondrial proteins has been shown to be among the earliest changes and this is associated with poor sarcolemmal repair (Rayavarapu et al., 2013; Vila et al., 2017).

To address the emerging questions about MICU's functional significance and potential disease-causing mechanisms in SM, we set up a comprehensive approach, including a SM-specific MICU1 knockout mouse model and MICU1-deficient patient-derived fibroblasts. We show that lack of MICU1 lowers the activation threshold for MCU-mediated Ca^{2+} uptake both in mouse myofibers and patient fibroblasts, which is reversed by MICU1 re-expression. Lack of MICU1 also alters the cellular Ca^{2+} homeostasis during myofiber contraction, and leads to increased signs of muscle atrophy, SM weakness, and fatigue. In myofibers with injured sarcolemma, lack of MICU1 inhibits repair by compromising mitochondrial Ca^{2+} uptake. MICU1 re-expression in patient cells enables efficient plasma membrane repair of these cells. These studies demonstrate the importance of the regulation of mitochondrial Ca^{2+} uptake in myofiber function and repair and offer mechanistic clues to the muscle disease of the MICU1-deficient patients.

RESULTS

MICU1-Patient Fibroblasts Show a Lower Activation Threshold for the mtCU Complex

To assess the physiological relevance of MICU1 in human cells, we obtained dermal fibroblasts from patients with homozygous MICU1 exon 1 deletion (MICU1-patient) (Lewis-Smith et al., 2016) and respective controls (CTRLs; CTRL1 and CTRL2). Using immunoblot analysis, we confirmed the previous report that the pathogenic patient mutation resulted in loss of MICU1 protein (Figure 1A). Other components of the mtCU, MICU2, MCU, and EMRE also showed decreases in patient fibroblasts compared to CTRL fibroblasts (Figure 1A).

At the transcript level, total MICU1 ($MICU1_{tot}$) mRNA in patient fibroblasts was greatly decreased relative to CTRLs (Figure 1B). However, mRNA levels of the other mtCU members—MICU2, MCU, and EMRE—were unchanged in the patient. These results suggest that loss of MICU1 might cause instability of some other proteins of the mtCU complex. Vecellio Reane and colleagues recently found that SM in mouse has a specific transcript variant that they named MICU1.1 (described as variant 2 in the NIH database nucleotide collection, and therefore called $MICU1_{V2}$ here) (Vecellio Reane et al., 2016). We

could not discriminate between transcripts of conventional $MICU1_{V1}$ and $MICU1_{V2}$ in the human cells, and measured only the amount of total MICU1. While quantifying the transcript levels of these isoforms, we also checked a third mRNA variant: $MICU1_{V3}$ (GenBank: NM_144822). This variant has a distinct 5′ UTR, which would cause translation initiation to occur at a start codon downstream to the other variants of MICU1 (NCBI). The predicted protein encoded by this transcript is shorter and has a unique N terminus. Notably, $MICU1_{V3}$ transcript is also decreased in the patient fibroblasts compared to CTRLs (Figure 1B).

To assess whether loss of MICU1 perturbs the cytoplasmic Ca^{2+} concentration ($[Ca^{2+}]_c$) dependence of the mtCU in the patient cells, we tested mitochondrial Ca^{2+} uptake. The plasma membrane was permeabilized with saponin (40 μg/ml) and experiments were performed in the presence of sarco/endoplasmic reticulum Ca^{2+}-ATPase (SERCA) inhibitor thapsigargin (Tg) and the mitochondrial Na^+/Ca^{2+} exchanger blocker CGP37157 to isolate the mtCU-mediated mitochondrial Ca^{2+} influx. Dependence of mitochondrial uptake rate on $[Ca^{2+}]_c$ is shown in the double-logarithmic plot (Figure 1C). In response to submicromolar $[Ca^{2+}]_c$ increases, patient mitochondria displayed Ca^{2+} uptake, whereas CTRL mitochondria showed little response. Furthermore, MICU1-patient showed significantly less cooperativity in mitochondrial Ca^{2+} uptake rate as a function of $[Ca^{2+}]_c$ than either of the CTRLs, as shown by the decreased slope of the double-logarithmic plot (slope = 0.99 ± 0.14 in MICU1-patient compared to 3.03 ± 0.64 for CTRL1 and 2.94 ± 0.18 for CTRL2, n = 4). Thus, MICU1-patient fibroblasts reproduced the loss of gatekeeping and loss of cooperativity in the mitochondrial Ca^{2+} uptake phenotype previously described in MICU1-deficient HeLa cells, mouse hepatocytes (Csordás et al., 2013), and mouse embryonic fibroblasts (MEFs) (Antony et al., 2016).

To further test the relevance of MICU1's loss in calcium signaling, we evaluated the $[Ca^{2+}]_c$- and mitochondrial-matrix-free $[Ca^{2+}]$ ($[Ca^{2+}]_m$) response during store-operated Ca^{2+} entry (SOCE) (Figures 1D and 1E). The ER Ca^{2+} store was pre-depleted by Tg while the cells were stored in a Ca^{2+}-free buffer. The rise in $[Ca^{2+}]_c$ induced by the addition of 1.5 mM $CaCl_2$ (Ca^{2+}) (Figure 1D) was similar in CTRL and MICU1-patient fibroblasts, generating a $[Ca^{2+}]_c$ peak around 250 nM in both cell lines (Figures 1D and 1F). Measurement of the corresponding $[Ca^{2+}]_m$ in CTRL cells showed no increase, indicating that the threshold for mtCU activation was not achieved. However, in patient cells a similar increase in $[Ca^{2+}]_c$ was followed by an increase in the $[Ca^{2+}]_m$ (Figures 1E and 1G). The specificity of changes associated with MICU1 loss in patient fibroblasts was validated by rescuing dysfunctional $[Ca^{2+}]_m$ homeostasis in patient cells by the expression of an MICU1 HA-tagged construct (MICU1-HA) (Figure 1H). The presence of MICU1-HA completely abolished the aberrant $[Ca^{2+}]_m$ response detected in MICU1-patient cells and restored the mitochondrial Ca^{2+} uptake threshold back to what was observed in CTRL fibroblasts. Acute overexpression of MCU and EMRE accelerated and augmented the $[Ca^{2+}]_m$ response in MICU1-patient cells (Figure S1), indicating that downregulation of these proteins caused a decrease in the functional mtCUs (Figures 1A and 1B), which likely contributed to a, presumably adaptive, decrease in the maximal mitochondrial Ca^{2+} influx (Figure 1C).

Knockout of MICU1 in Murine SM Impairs mtCU Calcium Thresholding

To create a stable, striated muscle-specific MICU1 knockout murine model (MICU1-smKO), C57Bl6 mice expressing Cre recombinase under the CK promoter (Ckmm-Cre) were crossed with mice with floxed MICU1 alleles ($MICU1^{F/F}$) (Antony et al., 2016). Ckmm-Cre has been shown to have specificity for striated muscle (Hauser et al., 2000). $MICU1^{F/F}$ mice were used as the CTRL. Efficient deletion of MICU1 was confirmed by immunoblot (Figure 2A) and qPCR analysis (Figure 2B). As in the human fibroblasts, levels of MCU and EMRE proteins were decreased by ~25% and ~50%, respectively ($p < 0.01$ versus CTRL for both), without a significant change in the transcript levels. In contrast to the fibroblasts, MICU2 protein was unchanged with MICU1 depletion. Notably, the abundance of MICU2 is constitutively low in SM relative to other tissues (Paillard et al., 2017). All transcript variants of MICU1, including the SM-specific variant $MICU1_{V2}$, were decreased. We also found a $MICU1_{V3}$ in the mouse SM and this was decreased in the MICU1-smKO mice. The mouse $MICU1_{v3}$ differed from the human $MICU1_{v3}$ as the mouse-specific variant lacks two alternate exons in the coding region compared to $MICU1_{V1}$. This causes the predicted mouse protein to be shorter than isoform 1, but with the same N- and C-termini as in isoform 1.

To test the mitochondrial Ca^{2+} handling in the myofibers of the MICU1-smKO mice, *flexor digitorum brevis* (FDB) muscle in CTRL and MICU1-smKO mice was electroporated with mitochondria-targeted RCaMP (mtRCaMP). After 7–10 days of expression, individual myofibers were isolated and loaded with fura2 to measure $[Ca^{2+}]_c$. The SOCE-induced $[Ca^{2+}]_c$ response was suppressed in MICU1-smKO (Figure S2A). As in the patient fibroblasts, the $[Ca^{2+}]_m$ response upon SOCE was evaluated in the myofibers (Figures 2C–2E). Plotting $[Ca^{2+}]_m$ against $[Ca^{2+}]_c$ in each myofiber revealed that CTRL myofibers regularly showed $[Ca^{2+}]_m$ rise once $[Ca^{2+}]_c$ attained 150 nM (Figure 2C), but in many MICU1-smKO myofibers, $[Ca^{2+}]_m$ increase was observed at $[Ca^{2+}]_c < 100$ nM (Figure 2D). Mean traces confirm a left-ward-shifted $[Ca^{2+}]_c$ dose response for MICU1-smKO relative to the CTRL (Figure 2E). A 10% increase in $[Ca^{2+}]_m$ could be achieved at $[Ca^{2+}]_c$ of 220 ± 2 nM in CTRL and at 120 ± 1 nM in the MICU1-smKO myofibers (Figure 2F). Altogether, these results support that MICU1 determines the $[Ca^{2+}]_c$ threshold for mtCU activation in SM, as reported for liver and heart (Antony et al., 2016; Csordás et al., 2013; Paillard et al., 2017).

MICU1 Ablation Alters the $[Ca^{2+}]_m$ Responses to Twitch and Tetanic Stimulation

Next, we evaluated whether ablation of MICU1 alters SM EC coupling–associated Ca^{2+} transients during twitch or repeated tetanic electrical stimulation (ES). $[Ca^{2+}]_c$ transients during twitch stimulation, measured using the Ca^{2+} dye fluo4, were similar between CTRL and MICU1-smKO mice (Figure 3A). Furthermore, the $[Ca^{2+}]_m$ levels measured using rhod2 dye were significantly decreased in MICU1-smKO myofibers during twitch stimulation (Figure 3B). Next, we measured absolute $[Ca^{2+}]_c$ levels in response to tetanic stimulation using fura2 that allows calibration of the absolute $[Ca^{2+}]_c$ levels. Baseline $[Ca^{2+}]_c$ (Figure S2B) and $[Ca^{2+}]_c$ transients in response to tetanic stimulation were similar for MICU1-smKO and CTRL though there was a tendency for smaller $[Ca^{2+}]_c$ transients in the smKO (Figure 3C). To perform ratiometric measurement of the $[Ca^{2+}]_m$ response in

myofibers, FDB muscles were co-transfected with the mitochondria-targeted Ca^{2+} sensor mtRCaMP and also mitochondria-targeted yellow fluorescence protein (mtYFP). At baseline, the mtRCaMP/mtYFP ratio was significantly elevated in myofibers lacking MICU1 (Figure S2C), indicating an elevated basal Ca^{2+} content. To further confirm high basal $[Ca^{2+}]_m$, we measured the $[Ca^{2+}]_c$ rise caused by Ca^{2+} discharge from the mitochondria induced with FCCP+oligomycin. This increase was larger in MICU1-smKO than in CTRL (Figure S2D), supporting that impaired gatekeeping resulted in mitochondrial Ca^{2+} overload. During tetanic stimulation, MICU1-smKO myofibers showed a smaller $[Ca^{2+}]_m$ response compared to CTRL mice, consistent with the observations during twitch stimulation (Figure 3D). Although the $[Ca^{2+}]_m$ peak might be underestimated because of the normalization to an elevated baseline, the suppression of the sustained phase of the $[Ca^{2+}]_m$ response is evidence for impaired mitochondrial Ca^{2+} delivery from SR to mitochondria in the contracting MICU1-deficient SM.

MICU1 Deficiency Is Associated with Proximal Muscle Weakness and Muscle Atrophy

Complete loss of mitochondrial Ca^{2+} uptake has been linked to impaired SM trophic responses (Mammucari et al., 2015). Therefore, we tested whether MICU1 ablation affected the size of the MICU1-smKO muscles. As has been reported in the MICU1-deficient patients (Logan et al., 2014), we observed that in the MICU1-smKO mice the mass of both the proximal muscles examined, quadriceps and triceps, was significantly decreased (Figure 4A). The mass of the other (distal) muscles and the total body mass was comparable between CTRL and MICU1-smKO (Figure S3A). Histological examination of myofiber size in two different muscles tibialis anterior (TA) and quadriceps from MICU1-depleted SM showed a trend toward an increased number of small myofibers (Figure 4B), as was observed when MCU was deleted in SM (Mammucari et al., 2015). This trend of smaller-sized myofibers in the MICU1-smKO muscle correlated with increased expression of the ubiquitin ligase involved in degradation of contractile proteins, Trim63/Murf-1, and of the atrophy-related muscle-specific ubiquitin ligase Fbxo32/Atrogin-1, indicating activation of myofiber atrophy (Figure 4C). To evaluate if a canonical Atrogin-1 and MURF-1 pathway is activated by MICU1 deficiency in the SM, we undertook immunoblot analysis to quantify the phosphorylated and total levels of AKT, S6, and AMPK proteins. Our analysis showed no detectable differences in this pathway between CTRL and MICU1-smKO (Figure S3C).

Muscle pathology such as muscular dystrophy is associated with a change in fiber-type distribution (Marshall et al., 1989; Pedemonte et al., 1999). Using antibodies against myosin heavy chain IIB (MHC-IIB), IIA (MHC-IIB), and 1 (MHC-I), no significant difference was found in fiber-type composition between CTRL and MICU1-smKO TA muscles: type IIB fibers were predominant (55%–65%), type IIA fibers were mildly frequent (5%–6%), and almost no (< 1%) MHC-I-positive fibers were detected, as previously reported for TA muscle in mice (Kammoun et al., 2014) (Figures S4A–S4D).

Evidence of possible changes in fiber-type distribution in human patients was observed by a reduction in NADH staining (Logan et al., 2014), indicative of mitochondrial dysfunction and loss of type 1 fibers. Consistent with this, we observed signs of mitochondrial dysfunction in MICU1-smKO mice by an overall reduction in NADH labeled fibers (Figure

S5A). However, when we immunoblotted for an established marker to each respiratory complex in the quadriceps muscle lysates, no difference was documented between MICU1-smKO and CTRL (Figure S5B). Thus, no significant change in the OXPHOS complexes supports the functional impairment revealed by the NADH labeling.

In view of the above indications of muscle atrophy, we next tested whether the lack of MICU1 protein affects muscle strength and endurance. *In vivo* measurement demonstrated reduced grip strength in both the forelimbs and hindlimbs of MICU1-smKO mice (Figures 4D and 4E). *In vivo* force measurement of the crural muscle group (TA and the extensor digitorum longus [EDL] muscle) showed that single-twitch stimulation (pulse width 0.2 ms) elicited a trend for a smaller response in MICU1-smKO mice (Figure 4F), and maximum force developed upon tetanic stimulation was clearly lower in MICU1-smKO mice compared to CTRL (Figure 4G). Next, mice were challenged *in vivo* with an exhaustion protocol on a treadmill. MICU1-smKO mice stayed on the belt less time than CTRL, but the difference was not significant (Figure 4H). Lack of elevated serum lactate at rest is a hallmark of MICU1-deficient patients, which is different from patients suffering from many other mitochondrial disease-induced myopathies. Therefore, we measured serum lactate at both rest and also after the treadmill running session. Serum lactate levels were comparable between CTRL and MICU1-smKO mice at rest (Figure 4I). However, when levels were measured in the same mice immediately after they ran on a treadmill until exhaustion, we observed higher serum lactate in MICU1-smKO compared to CTRL mice (Figure 4I). Altogether, these *in vivo* changes in the MICU1-smKO mice indicate both functional and structural impairments, involving atrophy. Furthermore, the enhanced anaerobic response to exercise indicates that MICU1 deletion hinders oxidative metabolism in meeting an increased demand.

MICU1 Is Required for Efficient Plasma Membrane Repair

Patients with MICU1 mutations have increased serum CK levels, suggestive of greater myofiber damage (Lewis-Smith et al., 2016). Consistent with this, we detected elevated resting serum CK levels in MICU1-smKO mice (Figure 5A). To determine whether increased serum CK may be due to degeneration of myofibers, we first quantified myofiber central nucleation, which is a measure of regenerating myofibers. We observed no difference in the amount of centrally nucleated myofibers in CTRL and MICU1-smKO mice, indicating that myofiber degeneration is not a driver of muscle pathology in MICU1-deficient mice (Figure S3B). In contrast to the longer-term process of myofiber regeneration, myofiber repair occurs on the timescale of minutes in response to physical damage to the sarcolemma. Previous work has also shown that mitochondrial Ca^{2+} uptake deficit is associated with poor repair of plasma membrane injury in myofibers (Horn et al., 2017). Thus, we next hypothesized that elevated serum CK in MICU1-smKO mice may be due to an inability to repair sarcolemmal injury. To directly test if MICU1-smKO mice show poor myofiber repair, we subjected mice to eccentric injury by downhill treadmill running (30°, running for 30 min). To assess myofiber damage due to physical activity, Evan's blue dye (EBD), which is excluded from intact myofibers, was intra-peritoneally injected in the mice prior to treadmill exercise. Twenty-four hours after eccentric exercise, *in vivo* muscle function was tested by running the mice on a level treadmill (no inclination). CTRL mice ran for 24.7 ± 6.7 min,

while the MICU1-smKO mice ran for 14.1 ± 3.1 min (Figure 5B). To assess if this reduction in the running capacity of the MICU1-smKO mice might reflect damaged myofibers, EBD labeling of myofibers was quantified in the quadriceps muscle. In CTRL mice, 3.6% ± 0.8% of myofibers were labeled with EBD, whereas this number in MICU1-smKO mice increased by over 5-fold to 18.8% ± 4.1% (Figures 5C and 5D). Altogether, these findings demonstrate that eccentric muscular activity results in increased myofiber damage in MICU1-smKO myofibers.

To isolate membrane repair capacity from injury magnitude, we next examined myofiber repair following focal sarcolemmal injury with a pulsed laser at the same laser power for each myofiber (Defour et al., 2014a). Myofibers in intact biceps muscle isolated from CTRL and MICU1-smKO mice were injured by a pulsed laser in the presence of a membrane impermeant dye (FM1-43). Dye entry into cells after injury ceases after the sarcolemmal injury is repaired, while poor repair leads to prolonged and hence greater dye entry. Thus, monitoring the extent and the kinetics of FM-dye entry following a controlled focal injury provides a direct measure of sarcolemmal repair ability. Compared to CTRL myofibers, injury to MICU1-smKO myofibers showed prolonged dye entry (Figures 5E and 5F). To assess whether or not an individual myofiber was able to repair successfully, we quantified FM-dye uptake 4 min after injury, a time after which membrane resealing should have occurred. Only in a cell that failed to repair should FM-dye still be increasing at this time. Using this method, we found that only 24.4% ± 4.7% of CTRL myofibers failed to repair from injury, while 50.7% ± 3.0% of MICU1-smKO myofibers failed to repair, demonstrating the poor repair ability of the MICU1-deficient myofibers (Figure 5G).

Mitochondrial dysfunction also compromises repair of other cells including fibroblasts (Horn et al., 2017). Thus, next we examined whether MICU1-patient fibroblasts also exhibit poor plasma membrane repair. Using the FM-dye-based focal laser injury assay described above for the myofibers, we observed that injured MICU1-patient fibroblasts also showed greater FM1-43 dye uptake compared to CTRL healthy human fibroblasts (Figure 5H). Further, the inability of MICU1-patient cells to repair was significantly higher than two CTRL human fibroblasts tested ($p < 0.05$; Figure 5I). To address if poor repair of the patient fibroblasts was due to the lack of MICU1 protein, patient fibroblasts were transiently transfected with an MICU1-HA expressing plasmid. Compared with MICU1-patient fibroblasts, MICU1-HA transfected patient fibroblasts showed reduced FM-dye entry, indicating their improved membrane repair kinetics (Figure 5J). Further, similar to the CTRL fibroblasts, only 24.3% ± 5.1% of the MICU1-HA-expressing patient fibroblasts failed to repair compared to ~40% of the MICU1-patient fibroblasts (Figure 5K). These results demonstrate that loss of MICU1 protein is sufficient to cause poor plasma membrane repair in mice and man alike, and occurs both in differentiated and highly specialized SM fibers as well as in proliferating cells in culture.

MICU1 Is Required for Mitochondrial Ca^{2+} Homeostasis during Sarcolemmal Repair

Poor sarcolemmal repair of MICU1 myofibers may be caused by mitochondrial Ca^{2+} uptake deficit in the injured myofibers. Therefore, we sought to better understand the connection between regulated mitochondrial Ca^{2+} uptake and membrane repair subsequent to

sarcolemmal injury. To measure the kinetics of the $[Ca^{2+}]$ increase after focal laser injury, individual FDB myofibers isolated from CTRL and MICU1-smKO mice were loaded with fluo4 and rhod2 to measure $[Ca^{2+}]_c$ and $[Ca^{2+}]_m$, respectively, in the same myofiber as it repaired from sarcolemmal damage. Injury caused Ca^{2+} entry from the extracellular space, resulting in an immediate increase in $[Ca^{2+}]_c$ (Figure 6A). There was no difference in the magnitude of injury-triggered increase in $[Ca^{2+}]_c$ or the time it took for $[Ca^{2+}]_c$to reach its peak in CTRL and MICU1-smKO mice (Figures 6B and 6C). However, clearing the injury-triggered increase in the $[Ca^{2+}]_c$ took nearly three times longer in MICU1-smKO myofibers than in the CTRL (Figure 6D).

Delayed clearance of the injury-triggered $[Ca^{2+}]_c$ increase suggested that loss of MICU1 diminishes the ability of mitochondria to take up the $[Ca^{2+}]_c$ increase caused by sarcolemmal injury. We previously showed that uptake of $[Ca^{2+}]_c$ by mitochondria triggers mitochondrial redox signaling that facilitates sarcolemmal repair (Horn et al., 2017). Given the role of MICU1 in the cooperative activation of the mtCU, we examined the injury-triggered uptake of Ca^{2+} by the mitochondria at peak $[Ca^{2+}]_c$ for CTRL and MICU1-smKO myofibers. At the peak of the injury-triggered increase in $[Ca^{2+}]_c$, CTRL myofibers showed a 1.6-fold increase in their $[Ca^{2+}]_m$ levels, and this increase was significantly less in MICU1-smKO (Figure 6E). Furthermore, as compared to the CTRL, the maximal injury-triggered increase in $[Ca^{2+}]_m$ level was also lower in the MICU1-smKO myofibers (Figure 6F). Finally, unlike the CTRL myofibers that reached a maximal $[Ca^{2+}]_m$ level in less than 2 s, MICU1-smKO myofibers were significantly delayed in reaching the maximal $[Ca^{2+}]_m$ level (Figure 6G). Altogether the above results demonstrate that loss of MICU1 suppresses the injury-triggered increase in $[Ca^{2+}]_m$ within the time window that is critical for the repair of injured sarcolemma.

DISCUSSION

We have determined the pathophysiological consequences of a disease-linked MICU1 loss-of-protein mutation in human fibroblasts as well as of MICU1 gene deletion in the SM of mice. The outcomes and the proposed underlying mechanism are depicted in Figure 7 and described in detail in the corresponding figure legend. Briefly, we demonstrated that loss of MICU1 in SM fibers affects the $[Ca^{2+}]_m$ transients during EC coupling and leads to less contractile force produced upon tetanic stimulation. MICU1-smKO mice show increased fatigue and impaired adaptation of aerobic metabolism upon exercise. There is increased muscle atrophy and, similar to the MICU1-patients, the loss of muscle mass is greater in the proximal muscles. Both MICU1-deficient SM and patient fibroblasts are also compromised in their ability to undergo plasma membrane repair. This deficit results from impaired handling of mitochondrial Ca^{2+} following plasma membrane injury. The mitochondrial Ca^{2+} uptake deficit and poor plasma membrane repair are both rescued by short-term expression of MICU1, establishing the direct causal relationship between these deficits. Thus, our mouse model phenocopies the patients' SM impairments, and demonstrates the dependence of exercise tolerance and SM growth and maintenance on how MCU is regulated, not merely on whether or not there is mitochondrial Ca^{2+} uptake. Furthermore, this work links the loss of control of mitochondrial Ca^{2+} to impaired adaptation of oxidative metabolism and

exhaustion, and reveals poor plasma membrane repair as a pathogenic mechanism for the clinical symptoms, which may be targetable for therapy.

Patient fibroblasts and the mouse SM display what appears to be a stereotypical rearrangement of multiple mtCU complex components upon loss of MICU1 (Figures 1 and 2). Loss of MICU1 protein is accompanied by a rearrangement of protein levels of mtCU components, specifically a decrease in EMRE and MCU, which would result in fewer constitutively active mtCU pores. It has been shown before that stable deletion of MICU1 is associated with decreased protein levels of other mtCU components including EMRE (Liu et al., 2016) and MICU2 (Kamer and Mootha, 2014; Sancak et al., 2013). But in some paradigms a different pattern has emerged, notably in some MICU1-deficient patients, EMRE is increased (Bhosale et al., 2017). Because we found no changes in the mRNA of EMRE and MCU that are downregulated at the protein level in the patient fibroblasts and MICU1KO SM (Figures 1 and 2), we propose that losing MICU1 results in a destabilized mtCU complex that favors the downregulation of some components. We hypothesize that an MICU1 deficit induces a negative feedback loop by increased mtCU Ca^{2+} flux at resting $[Ca^{2+}]_c$ levels, which suppresses the number of fully functional mtCU complexes and reduces the risk for Ca^{2+} overload that can initiate the mitochondrial cell death mechanism. The survival benefit of such a mechanism has been validated by EMRE deletion in MICU1-KO mice (Liu et al., 2016). Interestingly, when EMRE is expressed in excess, it can also inhibit the mtCU complex formation (Tsai et al., 2017) so the elevation of EMRE might also serve to suppress an augmented mtCU-mediated Ca^{2+} uptake. Nevertheless, the spectrum of adaptive mechanisms and their functional outcome in patients will require future studies involving more patients.

$[Ca^{2+}]_m$ is closely coupled to the $[Ca^{2+}]_c$ rise in the contracting SM, and the Ca^{2+} delivery to the mitochondria is dependent on the MCU (Pan et al., 2013; Rudolf et al., 2004). Our study reveals that resting $[Ca^{2+}]_m$ is higher in MICU1-deficient SM, likely as a consequence of impaired MCU gatekeeping (Figures 2E and S2C). Furthermore, the shape of the $[Ca^{2+}]_m$ response is determined by MICU1, and we find that the rise in $[Ca^{2+}]_m$ is reduced both in the twitch contraction and in the tetanic contraction paradigm. This might be caused either by the lack of cooperative activation of the MCU by $[Ca^{2+}]_c$ (Figure 1C), or by the compensatory downregulation of the pores formed by MCU and EMRE (Figure 2A). Thus, in SM, MICU1 contributes to the mitochondrial Ca^{2+} uptake pattern during both twitch and tetanic stimulations.

Because the $[Ca^{2+}]_c$ responses were not significantly altered in the MICU1-smKO under the same conditions, the changes in SM structure and function in this model might be due to the loss of control in $[Ca^{2+}]_m$ rather than that in $[Ca^{2+}]_c$.

To test the impact of $[Ca^{2+}]_m$ in muscle growth and contractile function, MCU has been targeted in several recent studies (Gherardi et al., 2019; Kwong et al., 2018; Mammucari et al., 2015). First, Mammucari et al. observed poor growth in SM upon silencing of MCU and linked this to impaired signaling through PGC1α and Akt. Complementing this, they reported enhanced growth upon overexpression of MCU due to increased PGC-1α4 and IGF1-Akt/PKB-dependent signaling (Mammucari et al., 2015). More recently, the same

authors reported constitutive and inducible MCU-smKO models showing decreased muscle performance, a fiber-type switch toward fast myosin heavy chains (MHCs), and a metabolic rewiring toward preferential fatty acid oxidation (Gherardi et al., 2019). Kwong et al. also created constitutive and inducible MCU-smKO models in which they reported no change in SM growth or maturation. However, they also observed a shift to fatty acid preference (Kwong et al., 2018). Both studies concluded that mitochondrial Ca^{2+} uptake determines the fuel selection but in terms of contractile function they inferred differently. For MICU1, whole body knockouts with muscle weakness have been reported but in this model it is difficult to determine the relative contribution of MICU1 deficiency in SM versus the nervous system and other tissues (Liu et al., 2016). In our SM-specific MICU1-deficient mice we show that signs of muscle weakness and early exhaustion during exercise are linked to impaired SM growth and increased markers of atrophy (Figure 4).

In terms of the mechanisms coupling the dysregulation of $[Ca^{2+}]_m$ to impaired maintenance and contractile function, we have two different leads. First, MICU1 loss has been shown to impair oxidative metabolism in hepatocytes and patient-derived cell lines, which has been attributed to ineffective activation of the Ca^{2+}-sensitive dehydrogenases and other enzymes in the mitochondrial matrix due to less $[Ca^{2+}]_m$ rise during $[Ca^{2+}]_c$ spikes and oscillations (Csordás et al., 2013; Logan et al., 2014). Consistent with this, we find that the MICU1-smKO mice show normal basal lactate levels, as observed in patients (Musa et al., 2019), but a greater rise upon exercise, which likely reflects the impaired adaptation of aerobic metabolism (Figure 4I). It seems plausible that dysregulation of the $[Ca^{2+}]_m$-dependent steps of oxidative metabolism would be relevant for muscle fatigue and weakness in the MICU1-smKO mice.

Other components of the MICU1-smKO phenotype and patient symptoms like the elevated serum CK cannot be explained by dysregulation of metabolic activity in SM. Our recent studies have identified a role of mitochondrial Ca^{2+} uptake in coordinating the repair of injured muscle fibers (Horn et al., 2017). Further, mitochondrial dysfunction leading to myofiber repair deficit is linked to the onset of muscle disease (Vila et al., 2017). We find here that the SM-specific MICU1-deficient mice poorly tolerate eccentric exercise, which causes myofiber injury, and they poorly repair their sarcolemmal damage. By targeted and controlled *ex vivo* non-mechanical and focal sarcolemmal injury, we find that it is the inefficient repair (and not other myofibrillar deficits) that compromise the ability of the myofibers lacking MICU1 to recover from eccentric exercise-induced damage. This compromised repair correlates with impaired mitochondrial uptake of the membrane-injury-triggered increase in $[Ca^{2+}]_c$. As MICU1 expression can reverse the plasma membrane repair defect seen in the patient cells, it indicates that the $[Ca^{2+}]_m$ uptake deficit is caused by the lack of MICU1 and not due to an unrelated deficit in the patient cells. This also indicates that the observed muscle damage and high CK that are a feature of the MICU1-deficient patients and the MICU1-smKO mouse, arise from impaired mitochondrial Ca^{2+} handling that then fails to support the maintenance of membrane integrity.

An important clinical signature of MICU1-patients is early-onset proximal muscle weakness, fluctuating fatigue, elevated serum CK levels upon stress, preserved fiber type but diffuse variations in fiber size, increased frequency of internal and central nuclei and clusters

of regenerating myofibers without pronounced fibrosis or fatty infiltration (Lewis-Smith et al., 2016; Logan et al., 2014). We systematically investigated these pathological features in MICU1-smKO mice that look outwardly normal and have normal body weight but show loss of mass in the proximal muscles: the quadriceps and triceps. The strength of several SM groups was decreased and serum CK levels were elevated. In the SM histology of a MICU1-patient, some atrophic myofibers were also noticed (Lewis-Smith et al., 2016). Consistent with this, we also document elevated atrophy markers in the MICU1-smKO mice. The similarity of the MICU1 SM mouse phenotype to the patient symptoms suggests that some of the human symptoms can be attributed directly to MICU1 loss in SM. However, some symptoms in the patients might be more severe than in the MICU1-deficient mice because patients also lack MICU1 in other cell types like the motor neurons; to better understand the neuronal component of the pathogenesis, a neuron-specific MICU1 knockout will be needed. Moreover, we anticipate that the pathology of the MICU1-smKO mice may be exacerbated by stress, as we previously showed with liver-specific knockout of MICU1 (Antony et al., 2016; Csordás et al., 2013). Further, use of the MICU1-smKO model and how it recapitulates patient symptoms may suggest avenues for developing and testing therapies for disease caused by MICU1 loss and possibly also for other mitochondrial myopathies associated with $[Ca^{2+}]_m$ dysregulation.

STAR★METHODS

LEAD CONTACT AND MATERIALS AVAILABILITY

Materials Availability Statement: Further information and requests for resources and reagents should be directed to and will be fulfilled by the Lead Contact, György Hajnóczky, M.D., Ph.D. (Gyorgy.Hajnoczky@Jefferson.edu). There are restrictions to the availability of the human fibroblasts from patients having mutations in *MICU1* due to the limited availability of these cells and their potential of these cells to be passaged.

EXPERIMENTAL MODEL AND SUBJECT DETAILS

Human Fibroblasts—Human fibroblasts were obtained from Newcastle University, Newcastle upon Tyne, United Kingdom. MICU1-patient cells were previously described (patient “IV:6” in Lewis-Smith et al., 2016). The patient is male and was 13 years old at sampling. The 2 controls were healthy females both age 26 (CTRL1, CTRL2) at sampling. Cells were cultured in Dulbecco’s modified Eagle’s medium (11965-118, Invitrogen) supplemented with 10% fetal bovine serum, 2 mM glutamine and 100 U/ml penicillin and 100 μg/ml streptomycin in humidified air (5% CO2) at 37°C. Transfection of the cells was performed with plasmid DNA using Lipofectamine 3000 (Invitrogen) for 24-48h following manufacturer’s instructions.

Generation of the MICU1-smKO Mice—Mice were used in accordance with mandated standards of care and were approved by the Thomas Jefferson University Institutional Animal Care and Use Committee. To obtain MICU1-smKO, the Cre-loxP system was used to target exon 3 of the MICU1 gene for removal. Homozygous MICU1-floxed ($MICU1^{F/F}$) mice (on C56BL/6J background) were previously described (Antony et al., 2016). $MICU1^{F/F}$mice were then bred with B6-Tg(Ckmm-Cre) (C56BL/6J background, Jackson

Laboratory) mice in which Cre recombinase is driven by the muscle creatine kinase promoter Tg(Ckmm-Cre). These offspring were bred with homozygous MICU1$^{F/F}$ mice to establish homozygous MICU1$^{F/F}$ carrying the CKM-cre (MICU1-smKO) transgene. Genotype of mice was determined using the following primer pairs: 1–5′-GGTGGAGTCAAAGGGAGGAACAG-3′, and 2–5′-GCCCCATCTATGATAATGTTAAGC-3′ for floxed alleles, 3–5′-CAGAACCTGAAGATGTTCGC-3′ and 4–5′TACACCTCGGTGCTAACCAG-3′ for Tg(Ckmm-Cre) sequence. Both male and female mice, 6-8 month of age were used for the experiments.

METHOD DETAILS

***In Vivo* Electroporation and Harvesting of FDB Fibers for Electrical Stimulation—**Transfection of plasmids in FDB muscles of adult mice was performed as described (DiFranco et al., 2009). In brief, mice were anesthetized using 5% isoflurane, footpads were injected with 2 mg/ml hyaluronidase type IV (Sigma-Aldrich), and 1 h later, ~20 μg total cDNA was injected (10 μl) followed by electroporation using acupuncture needles as electrodes and delivering 20 pulses of 60 V and 30-ms duration at 1 Hz using a square pulse stimulator (model SD9; Grass Technologies) visualized with an oscilloscope (model TDS 220; Tektronix). Six–10 d after electroporation, mice were euthanized and FDB muscles were harvested. Muscles were digested using 4 mg/ml collagenase type 2 (16101015, ThermoFisher) for 1 h at 36°C under agitation, followed by mechanical dissociation, adapted from Casas et al. (2010). Isolated fibers were plated onto Matrigel (BD Biosciences)-coated coverslips in DMEM medium supplemented with Pen/Strep and 10% horse serum (HS), and used within 24 h after plating.

Biochemical Analysis—For western blotting of human fibroblasts, cell lysates were prepared in RIPA buffer supplemented with protease inhibitors (leupetin, antipain, pepstatin, phenylmethyl sulphonyl fluoride, Sigma). For western blotting from mouse samples, skeletal muscle was harvested then homogenized in RIPA buffer or mitochondria were first isolated from skeletal muscles from all limbs as previously described (Seifert et al., 2008) and then lysed in RIPA buffer as done for the cells. The following antibodies were used for primary overnight incubation: MICU1 (Sigma (Sg)–HPA036480, 1:400), MICU2 (Abcam (Ab)–ab101465, 1:500), MCU (Sg–HPA016480, 1:500); EMRE (Santa Cruz Biotechnology–sc86336, 1:500), Total-Oxphos (ab110411, 1:500), GRB2 (ab2234, 1:1000), pAMPK (2535S, 1:1000), AMPK (Cell Signaling Technology (CST)-2532S, 1:1000), pAKT (CST-9271S), AKT (9272S), pS6 (CST-2211S), S6 (CST-2217S) and Hsp60 (Thermo Scientific-MA3-028, 1:1000). Quantification was done using ImageJ (NIH).

RNA Isolation, cDNA Preparation and Quantitative PCR (qPCR)—Total RNA was isolated from frozen mouse quadriceps muscle using Animal Tissue RNA Purification Kit (Norgen Biotek) and from human fibroblasts using TRIzol reagent (Ambion). RNA concentration was measured by ND-1000 (NanoDrop). cDNA was synthesized using SuperScript III (Invitrogen) and used for qPCR reactions using SYBR Green (Invitrogen) on an ABI Prism 6000 sequence detection system (Life Technologies). Data were analyzed

using the comparative ΔΔCt method. Ct of the gene of interest was normalized tox that of β-actin. Primers used are listed in Table S1.

Fluorometric Measurements and Live-Cell Imaging—Fluorometric measurements of $[Ca^{2+}]_c$ clearance were performed as described (Csordás et al., 2013). Briefly, saponin-permeabilized fibroblasts (2.4 mg) were resuspended in 1.5 ml of intracellular medium containing 120 mM KCl, 10 mM NaCl, 1 mM KH_2PO_4,20mM Tris-HEPES at pH 7.2, and supplemented with protease inhibitors (leupetin, antipain, pepstatin, 1 μg ml^{-1} each), 2 mM MgATP, 2 μM Tg (Enzo) and maintained in a stirred thermostated cuvette at 36 °C. Assays were performed in the presence of 20 μM CGP-36156 (Enzo) and 2 mM succinate using a multiwavelength-excitation dual-wavelength-emission fluorimeter (DeltaRAM, PTI). The extramitochondrial Ca^{2+} concentration $[Ca^{2+}]_c$ was assessed using the ratiometric Ca^{2+} probe fura2/FA (1.5 μM, Teflabs) or fura-lowAff (formerly fura/FF; 1 μM, Teflabs). Fura fluorescence was recorded using 340–380 nm excitation and 510 nm emission. Calibration of the fura signal was carried out at the end of each measurement, adding 1 mM $CaCl_2$, followed by 10 mM EGTA/Tris, pH 8.5.

For imaging experiments, the cells were pre-incubated and loaded with fura2/AM in a serum-free extracellular medium (ECM, 121 mM NaCl, 5 mM NaHCO3, 10 mM Na-HEPES, 4.6 mM KCl, 1.2 mM KH2PO4, 1.2 mM MgSO4, 2mM CaCl2, 10 mM glucose, pH7.4) containing 2% BSA. For SOCE experiments ER stores were depleted by 10 min pretreatment with 2 μM Tg in Ca^{2+}-free buffer. When both $[Ca^{2+}]_c$ and $[Ca^{2+}]_m$ were recorded, excitation filters were as follows: 340/30nm, 380/20nm for fura2, 490/20nm for mtCepia for human cell lines, or 540/50nm for mtRCaMP and 490/20nm for mtYFP in the case of SM fibers. Data were acquired every 500ms for SOCE and 133ms for fibers ES. Imaging of human fibroblasts was performed using an inverted microscope (40 ×, DMRE 2; Leica), UApo objective (Olympus), and a CCD camera (ProEM 1024 EMCCD camera, Princeton Instruments), while recording of skeletal muscle fibers was carried out on an Olympus IX70 with UAPO 40 × oil 1.3 NA lens. The fura2 ratios were calibrated in terms of nM $[Ca^{2+}]_c$, whereas the mtCepia and mtRCaMP or mtYFP fluorescence at each time point was normalized to the initial fluorescence (F/F_0).

Myofiber Contraction and Calcium Quantification after Electrical Stimulation and Sarcolemmal Injury—Strips of FDB muscle from 8 month old male mice were placed in 0.2% collagenase in minimal essential media (MEM) with 10% fetal bovine serum and 1% penicillin/streptomycin (MEM/FBS media) and allowed to digest 3-4 h in an incubator (37°C, 95% O_2-5% CO_2). After 3-4 h, fibers were triturated in MEM/FBS media then left in the incubator until used for experiments. Fibers were assessed for changes in excitation-contraction coupling within 48h of isolation.

For excitation-contraction coupling measurements during twitch stimulation, fibers were loaded with fluo4/AM (10 μM, Life Technologies) and rhod2/AM (1 μM) dye in MEM/FBS media for 15 min at room temperature. Media containing dye was then removed by quick centrifugation, and fibers were resuspended in fresh MEM/FBS media. Fibers were then placed in a culture/stimulation chamber (Cell MicroControls) containing parallel electrodes on top of a microscope stage. In the chamber, fibers were continuously perfused with a

stimulating tyrode solution (121 mM NaCl, 5 mM KCl, 1.8 mM $CaCl_2$, 0.5 mM $MgCl_2$, 0.4 mM NaH_2PO_4, 24 mM $NaHCO_3$, and 5.5 mM glucose - pH 7.3). In this preparation, single fibers were unloaded and underwent shortening during electrical activation. All single fiber data were collected at room temperature (23°C). Single muscle fibers were stimulated at 1Hz (Square Pulse Stimulator, GRASS Technologies) with 1-min rest between stimulations. Images were acquired using an inverted IX81 microscope (Olympus America) custom equipped with a CSU-X1 spinning disc confocal unit (Yokogawa Electric Corp.). Image acquisition was controlled using Slidebook 6.0 (Intelligent Imaging Innovations Inc.) and images were acquired for 20ms every 500ms. $[Ca^{2+}]_c$ and $[Ca^{2+}]_m$ were measured as the change in fluorescence over the initial fluorescence (F/F_0).

For imaging $[Ca^{2+}]_m$ simultaneously with $[Ca^{2+}]_c$ in SM during tetanic stimulation, mtRCaMP/mtYFP transfected fibers were loaded with fura2/AM. Isolated FDB fibers were electrically stimulated by means of field stimulation as previously described (Eisner et al., 2014) with the following protocol of stimulation: 100tetani, 100 Hz, for 500 ms every 2.5 s, pulse length 2 ms in a custom-made chamber (1 ml, holding two parallel platinum electrodes positioned on each side of the light path, 1 cm apart from each other) connected to a square pulse stimulator and oscilloscope. The repetitive tetanus frequency was commanded by an external custom-designed microcontroller. Images (12 triplets/s) were acquired using ex: 340 and 380 nm for fura2 and ex: 545 nm for mtRCaMP, 488 for mtYFP and a dual band emission filter at a custom built epifluorescence imaging system. For measurement of $[Ca^{2+}]_c$ and $[Ca^{2+}]_m$ following focal sarcolemmal injury, isolated FDB myofibers were incubated with fluo-4 AM (10 μM, Life Technologies) and rhod-2 (1 μM) dye in MEM/FBS media for 15 min at room temperature. After washing with pre-warmed Tyrode media, myofibers were quickly centrifuged, placed on the microscope stage maintained at 37°C, and injured following the protocol for membrane injury described below. $[Ca^{2+}]_c$ and $[Ca^{2+}]_m$ were measured as the change in fluorescence over the initial fluo-4 fluorescence (F/F_0).

Measurements of Muscular Contractile Function *In Vivo*—Male mice were anaesthetized using 4%–5% isoflurane and then ~2% isoflurane via a nosecone for maintenance, (both with 1-1.5L/min 100% O_2). Rymadil (5mg/kg) was administered before starting the procedure. Briefly, the mouse was kept supine on a heated limb platform with clamps for affixing the limb. The leg was secured bent in a L shape in the limb plate using a sharpened screw positioned at the level of the knee. The foot was placed in the footplate, orthogonal to the tibia. Using a transcutaneous electrode, TA muscle was stimulated and force during plantarflexion was recorded (1300A system, Aurora Scientific Inc.). An *in vivo* stimulation protocol of a twitch (initial delay 0.2 s, pulse width 0.2ms) followed by a tetanus (initial delay 0.2 s, pulse frequency 65 Hz, pulse width 0.2ms, duration 0.8 s) repeated 3 times with a 60 s rest interval was applied.

Treadmill Running and Eccentric Exercise—The Columbus Instruments Exer 3/6 Treadmill was used to challenge male mice to controlled exercise. An acclimatizing period of 3 days was performed before evaluating the endurance of mice. Running was induced through application of a mild electrical stimulus (16–28 V). To induce running until

exhaustion, the treadmill speed was progressively increased from an initial belt speed of 12 m/min to a maximum of 22 m/min. Mice were considered exhausted when they remain on the shock grid for more than ≥ 5 s without attempting to get back onto the treadmill. Blood lactate levels were measured with a Lactate Plus Meter device (Nova Biomedical) at rest and immediately after the mouse had stopped running.

To induce *in vivo* eccentric muscle injury, male mice (6–8 months old) were run on a declined treadmill (Columbus Instruments, Columbus, OH, USA). The treadmill was maintained at a 30° decline and operated at a speed of 8 m/min for 30 minutes with prodding as needed to ensure continuous participation. To assess the impact of exercise-induced injury on spontaneous activity, mice were allowed to run freely on a flat treadmill (not inclined) 24 hours after eccentric exercise. Mice were run at a speed of 12 m/min until fatigued, indicated by the time at which the mouse stopped running after 5 successive bouts of prodding at least 30 s apart. For quantification of serum CK, blood was collected by retro orbital sinus puncture 24 hours prior to exercise and again post-exercise. Blood was centrifuged at 2000 RPM for 15 min at 4°C and serum was isolated. CK was measured using the EnzyChrome Creatine Kinase Assay Kit (ECPK-100, BioAssay Systems, Hayward, CA, USA) as per manufacturer's instructions. For quantification of muscle injury and repair, mice were injected with Evan's Blue Dye (EBD) 5 hours prior to eccentric exercise and quadriceps muscles were collected after euthanizing, 24 hours post-exercise. Tissues were sectioned at 8 μm on a Leica CM1900 cryostat. Wheat germ agglutinin (WGA) conjugated to Alexa Fluor 488 (Life Technologies, MA) was prepared as 1 mg/ml stock solutions and used at 1:500 dilution in PBS. Sections were mounted with Prolong Gold Mounting Media (Life Technologies, MA) with DAPI for nuclear staining. Microscopy was performed using an Olympus BX61 VS120-S5 Virtual Slide Scanning System with UPlanSApo 40X/0.95 objective, Olympus XM10 monochrome camera, and Olympus VS-ASW FL 2.7 imaging software. Images were analyzed using Olympus CellSens 1.13 and ImageJ software.

Grip Strength Measurement—Forelimb and hindlimb grip strength were assessed in 7-8 month old female mice using a grip strength meter as previously described (Spurney et al., 2009) (Columbus Instruments, Columbus, OH, USA). Mice were acclimated for three consecutive days prior to measurement. An average of five replicates for forelimb and hindlimb was taken for each animal.

Plasma Membrane Repair Assay—Human fibroblasts cultured on coverslips were transferred to Cellular Imaging Medium [CIM; Hanks' balanced salt solution with 10 mM HEPES, 2 mM $CaCl_2$ (pH 7.4)] and placed in a Tokai Hit microscopy stage-top ZILCS incubator (Tokai Hit Co.) maintained at 37°C. For laser injury, a 1- to 2-mm^2 area was irradiated for 10 ms with a pulsed laser (Ablate!, 3i Intelligent Imaging Innovations Inc.). Cells were imaged using an inverted IX81 microscope (Olympus America) custom equipped with a CSU-X1 spinning disc confocal unit (Yokogawa Electric Corp.). Images were acquired using Evolve 512 EMCCD (Photometrics) at 1 Hz. Image acquisition and laser injury was controlled using Slidebook 6.0 (Intelligent Imaging Innovations Inc.). For quantification of plasma membrane, FM1–43 dye (1 mg/ml, Life Technologies) was added to CIM before injury. FM dye intensity (F/F_0, where F_0 represents baseline fluorescence)

was used to calculate the kinetics of repair. Repair was determined by the entry of FM dye into the cell interior, where a plateau in FM dye increase indicated successful repair and failure to repair was indicated by unabated FM dye fluorescence increase. For *ex vivo* injury of myofibers from intact biceps muscle, mice were euthanized by CO_2 asphyxiation and muscles were immediately dissected. Whole biceps muscles were mounted in prewarmed Tyrode's buffer [119 mM NaCl, 5 mM KCl, 25 mM HEPES buffer, 2 mM $CaCl_2$, 2 mM $MgCl_2$, glucose (6 g/liter) (pH 7.4)] and imaged using the IX81 Olympus microscope as described above.

Histology—Histology and fiber type staining were performed on TA sections as previously described (Dyar et al., 2013). Hematoxylin/eosin staining was performed at the translational research /pathology shared resource at Thomas Jefferson University. Bright field images were acquired using a Zeiss Axio Observer microscope with DFC420 digital camera (Leica). NADH staining was performed using NADH (Sigma-Aldrich, St. Louis, MO; 8 mg/5 ml) and Nitro-blue tetrazolium (Sigma-Aldrich, St. Louis, MO; 2 mg/ml). Microscopy was performed using an Olympus BX61 VS120-S5 Virtual Slide Scanning System with UPlanSApo 40X/0.95 objective, Olympus XM10 monochrome camera, and Olympus VS-ASW FL 2.7 imaging software. Images were analyzed using Olympus CellSens 1.13 software. Fibers' Feret's diameter and cross-sectional area were calculated using ImageJ.

Fiber type staining was performed using anti-laminin antibody (sigma L9393) and the following myosin-heavy chain specific antibodies: BA-D5 (IgG2b, supernatant, 1:100 dilution, specific for MyHC-I; SC-71 (IgG1, supernatant, 1:100 dilution) specific for MyHC-2A; BF-F3 (IgM, purified antibody, 1:100 dilution) specific for MyHC-2B (Developmental Studies Hybridoma Bank). Secondary antibodies were as follows: chicken anti-rabbit Alexa Fluor 488 (A21441, Invitrogen to bind laminin), conjugated to DyLight488 fluorophore (to bind either to SC-61 or to BF-F3); goat anti-mouse IgG Alexa Fluor 647 conjugated to DyLight405 fluorophore (to bind to BA-D5). Image acquisition was performed using 488 nm, 561 nm and 638 laser lines of an LSM780 confocal laser-scanning microscope [20 × /1.4 NA, PlanApo (Carl Zeiss)]. Image analysis was done using ImageJ software.

QUANTIFICATION AND STATISTICAL ANALYSIS

Image acquisition and analysis were performed using Slidebook 6.0 or ImageJ software. The statistical analysis was carried out using the GraphPad Prism Software or SigmaPlot. For all kinetic trace data, individual time points were compared across all cells to determine significance by unpaired Student's t test. For all data, the D'Agostino and Pearson omnibus normality test was performed before determining the appropriate statistical test. For pairwise comparisons, unpaired t tests were used for all normally distributed data, whereas Mann-Whitney tests were used for nonparametric data. For multiple comparisons, ANOVA followed by Dunnett's post hoc test was used to determine significance of normally distributed data. For nonparametric multiple comparisons, a Kruskal-Wallis test followed by Dunn's multiple comparison test was used to determine significance ($p < 0.05$). In all cases, data not indicated as significant should be considered not statistically different. Replicate information is indicated in the figure legends.

DATA AND CODE AVAILABILITY

Data and Code Availability Statement: The published article includes all [datasets/code] generated or analyzed during this study.

Supplementary Material

Refer to Web version on PubMed Central for supplementary material.

ACKNOWLEDGMENTS

The authors thank Veronica Eisnerand David Weaver for help in setting up the imaging in myofibers and data analysis. J.K.J. acknowledges support by NIH grants (R01AR55686 and U54HD090257). A.H. and D.A.M. acknowledge support by NIAMS grant T32AR056993. The study at MitoCare was funded by an NIH grant (RO1 GM102724)to G.H. G.H. acknowledges funding by Foundation Leducq.

REFERENCES

Angelin A, Bonaldo P, and Bernardi P (2008). Altered threshold of the mitochondrial permeability transition pore in Ullrich congenital muscular dystrophy. Biochim. Biophys. Acta 1777, 893–896. [PubMed: 18435905]

Antony AN, Paillard M, Moffat C, Juskeviciute E, Correnti J, Bolon B, Rubin E, Csordás G, Seifert EL, Hoek JB, and Hajnóczky G (2016). MICU1 regulation of mitochondrial Ca(2+) uptake dictates survival and tissue regeneration. Nat. Commun 7, 10955. [PubMed: 26956930]

Bansal D, Miyake K, Vogel SS, Groh S, Chen CC, Williamson R, McNeil PL, and Campbell KP (2003). Defective membrane repair in dysferlin-deficient muscular dystrophy. Nature 423, 168–172. [PubMed: 12736685]

Baughman JM, Perocchi F, Girgis HS, Plovanich M, Belcher-Timme CA, Sancak Y, Bao XR, Strittmatter L, Goldberger O, Bogorad RL, et al. (2011). Integrative genomics identifies MCU as an essential component of the mitochondrial calcium uniporter. Nature 476, 341–345. [PubMed: 21685886]

Bhosale G, Sharpe JA, Koh A, Kouli A, Szabadkai G, and Duchen MR (2017). Pathological consequences of MICU1 mutations on mitochondrial calcium signalling and bioenergetics. Biochim Biophys Acta Mol Cell Res 1864, 1009–1017. [PubMed: 28132899]

Boncompagni S, Rossi AE, Micaroni M, Hamilton SL, Dirksen RT, Franzini-Armstrong C, and Protasi F (2009). Characterization and temporal development of cores in a mouse model of malignant hyperthermia. Proc. Natl. Acad. Sci. USA 106, 21996–22001. [PubMed: 19966218]

Casas M, Figueroa R, Jorquera G, Escobar M, Molgó J, and Jaimovich E (2010). IP(3)-dependent, post-tetanic calcium transients induced by electrostimulation of adult skeletal muscle fibers. J. Gen. Physiol 136, 455–467. [PubMed: 20837675]

Cooper ST, and Head SI (2015). Membrane Injury and Repair in the Muscular Dystrophies. Neuroscientist 21, 653–668. [PubMed: 25406223]

Csordás G, Golenár T, Seifert EL, Kamer KJ, Sancak Y, Perocchi F, Moffat C, Weaver D, de la Fuente Perez S, Bogorad R, et al. (2013). MICU1 controls both the threshold and cooperative activation of the mitochondrial Ca^{2+} uniporter. Cell Metab. 17, 976–987. [PubMed: 23747253]

De Stefani D, Raffaello A, Teardo E, Szabó I, and Rizzuto R (2011). A forty-kilodalton protein of the inner membrane is the mitochondrial calcium uniporter. Nature 476, 336–340. [PubMed: 21685888]

Defour A, Sreetama SC, and Jaiswal JK (2014a). Imaging cell membrane injury and subcellular processes involved in repair. J. Vis. Exp (85)

Defour A, Van der Meulen JH, Bhat R, Bigot A, Bashir R, Nagaraju K, and Jaiswal JK (2014b). Dysferlin regulates cell membrane repair by facilitating injury-triggered acid sphingomyelinase secretion. Cell Death Dis. 5, e1306. [PubMed: 24967968]

DiFranco M, Quinonez M, Capote J, and Vergara J (2009). DNA transfection of mammalian skeletal muscles using in vivo electroporation. J. Vis. Exp (32), 1520. [PubMed: 19841615]

Durham WJ, Aracena-Parks P, Long C, Rossi AE, Goonasekera SA, Boncompagni S, Galvan DL, Gilman CP, Baker MR, Shirokova N, et al. (2008). RyR1 S-nitrosylation underlies environmental heat stroke and sudden death in Y522S RyR1 knockin mice. Cell 133, 53–65. [PubMed: 18394989]

Dyar KA, Ciciliot S, Wright LE, Biensø RS, Tagliazucchi GM, Patel VR, Forcato M, Paz MI, Gudiksen A, Solagna F, et al. (2013). Muscle insulin sensitivity and glucose metabolism are controlled by the intrinsic muscle clock. Mol. Metab 3, 29–41. [PubMed: 24567902]

Eisner V, Csordás G, and Hajnóczky G (2013). Interactions between sarco-endoplasmic reticulum and mitochondria in cardiac and skeletal muscle - pivotal roles in Ca^{2+} and reactive oxygen species signaling. J. Cell Sci 126, 2965–2978. [PubMed: 23843617]

Eisner V, Lenaers G, and Hajnóczky G (2014). Mitochondrial fusion is frequent in skeletal muscle and supports excitation-contraction coupling. J. Cell Biol 205, 179–195. [PubMed: 24751540]

Fieni F, Lee SB, Jan YN, and Kirichok Y (2012). Activity of the mitochondrial calcium uniportervaries greatly between tissues. Nat. Commun 3,1317. [PubMed: 23271651]

Franzini-Armstrong C (2018). The relationship between form and function throughout the history of excitation-contraction coupling. J. Gen. Physiol 150, 189–210. [PubMed: 29317466]

Gherardi G, Nogara L, Ciciliot S, Fadini GP, Blaauw B, Braghetta P, Bonaldo P, De Stefani D, Rizzuto R, and Mammucari C (2019). Loss of mitochondrial calcium uniporter rewires skeletal muscle metabolism and substrate preference. Cell Death Differ. 26, 362–381. [PubMed: 30232375]

Hauser MA, Robinson A, Hartigan-O'Connor D, Williams-Gregory DA, Buskin JN, Apone S, Kirk CJ, Hardy S, Hauschka SD, and Chamberlain JS (2000). Analysis of muscle creatine kinase regulatory elements in recombinant adenoviral vectors. Mol. Ther 2, 16–25. [PubMed: 10899824]

Hernández-Ochoa EO, Pratt SJP, Lovering RM, and Schneider MF (2016). Critical Role of Intracellular RyR1 Calcium Release Channels in Skeletal Muscle Function and Disease. Front. Physiol 6, 420. [PubMed: 26793121]

Horn A, Van der Meulen JH, Defour A, Hogarth M, Sreetama SC, Reed A, Scheffer L, Chandel NS, and Jaiswal JK (2017). Mitochondrial redox signaling enables repair of injured skeletal muscle cells. Sci. Signal 10, eaaj1978. [PubMed: 28874604]

Jouaville LS, Pinton P, Bastianutto C, Rutter GA, and Rizzuto R (1999). Regulation of mitochondrial ATP synthesis by calcium: evidence for a longterm metabolic priming. Proc. Natl. Acad. Sci. USA 96, 13807–13812. [PubMed: 10570154]

Kamer KJ, and Mootha VK (2014). MICU1 and MICU2 play nonredundant roles in the regulation of the mitochondrial calcium uniporter. EMBO Rep. 15, 299–307. [PubMed: 24503055]

Kammoun M, Cassar-Malek I, Meunier B, and Picard B (2014). A simplified immunohistochemical classification of skeletal muscle fibres in mouse. Eur. J. Histochem 58, 2254. [PubMed: 24998919]

Kwong JQ, Huo J, Bround MJ, Boyer JG, Schwanekamp JA, Ghazal N, Maxwell JT, Jang YC, Khuchua Z, Shi K, et al. (2018). The mitochondrial calcium uniporter underlies metabolic fuel preference in skeletal muscle. JCI Insight 3, 121689. [PubMed: 30429366]

Lewis-Smith D, Kamer KJ, Griffin H, Childs AM, Pysden K, Titov D, Duff J, Pyle A, Taylor RW, Yu-Wai-Man P, et al. (2016). Homozygous deletion in MICU1 presenting with fatigue and lethargy in childhood. Neurol. Genet 2, e59. [PubMed: 27123478]

Liu JC, Liu J, Holmström KM, Menazza S, Parks RJ, Fergusson MM, Yu ZX, Springer DA, Halsey C, Liu C, et al. (2016). MICU1 Serves as a Molecular Gatekeeper to Prevent In Vivo Mitochondrial Calcium Overload. Cell Rep. 16, 1561–1573. [PubMed: 27477272]

Logan CV, Szabadkai G, Sharpe JA, Parry DA, Torelli S, Childs AM, Kriek M, Phadke R, Johnson CA, Roberts NY, et al.; UK10K Consortium (2014). Loss-of-function mutations in MICU1 cause a brain and muscle disorder-linked to primary alterations in mitochondrial calcium signaling. Nat. Genet 46, 188–193. [PubMed: 24336167]

Mallilankaraman K, Doonan P, Cárdenas C, Chandramoorthy HC, Müller M, Miller R, Hoffman NE, Gandhirajan RK, Molgó J, Birnbaum MJ, et al. (2012). MICU1 is an essential gatekeeper for MCU-mediated mitochondrial Ca(2+) uptake that regulates cell survival. Cell 151, 630–644. [PubMed: 23101630]

Mammucari C, Gherardi G, Zamparo I, Raffaello A, Boncompagni S, Chemello F, Cagnin S, Braga A, Zanin S, Pallafacchina G, et al. (2015). The mitochondrial calcium uniporter controls skeletal muscle trophism in vivo. Cell Rep. 10, 1269–1279. [PubMed: 25732818]

Marshall PA, Williams PE, and Goldspink G (1989). Accumulation of collagen and altered fiber-type ratios as indicators of abnormal muscle gene expression in the mdx dystrophic mouse. Muscle Nerve 12, 528–537. [PubMed: 2779602]

McGreevy JW, Hakim CH, McIntosh MA, and Duan D (2015). Animal models of Duchenne muscular dystrophy: from basic mechanisms to gene therapy. Dis. Model. Mech 8, 195–213. [PubMed: 25740330]

Murphy E, Pan X, Nguyen T, Liu J, Holmström KM, and Finkel T (2014). Unresolved questions from the analysis of mice lacking MCU expression. Biochem. Biophys. Res. Commun 449, 384–385. [PubMed: 24792186]

Musa S, Eyaid W, Kamer K, Ali R, Al-Mureikhi M, Shahbeck N, Al Mesaifri F, Makhseed N, Mohamed Z, AlShehhi WA, et al. (2019). A Middle Eastern Founder Mutation Expands the Genotypic and Phenotypic Spectrum of Mitochondrial MICU1 Deficiency: A Report of 13 Patients. JIMD Rep. 43, 79–83. [PubMed: 29721912]

Paillard M, Csordás G, Szanda G, Golenár T, Debattisti V, Bartok A, Wang N, Moffat C, Seifert EL, Spät A, and Hajnóczky G (2017). Tissue-Specific Mitochondrial Decoding of Cytoplasmic Ca^{2+} Signals Is Controlled by the Stoichiometry of MICU1/2 and MCU. Cell Rep. 18, 2291–2300. [PubMed: 28273446]

Pan X, Liu J, Nguyen T, Liu C, Sun J, Teng Y, Fergusson MM, Rovira II, Allen M, Springer DA, et al. (2013). The physiological role of mitochondrial calcium revealed by mice lacking the mitochondrial calcium uniporter. Nat. Cell Biol 15, 1464–1472. [PubMed: 24212091]

Patron M, Checchetto V, Raffaello A, Teardo E, Vecellio Reane D, Mantoan M, Granatiero V, Szabó I, De Stefani D, and Rizzuto R (2014). MICU1 and MICU2 finely tune the mitochondrial Ca2+ uniporter by exerting opposite effects on MCU activity. Mol. Cell 53, 726–737. [PubMed: 24560927]

Pedemonte M, Sandri C, Schiaffino S, and Minetti C (1999). Early decrease of IIx myosin heavy chain transcripts in Duchenne muscular dystrophy. Biochem. Biophys. Res. Commun. 255, 466–469. [PubMed: 10049732]

Perocchi F, Gohil VM, Girgis HS, Bao XR, McCombs JE, Palmer AE, and Mootha VK (2010). MICU1 encodes a mitochondrial EF hand protein required for Ca(2+) uptake. Nature 467, 291–296. [PubMed: 20693986]

Plovanich M, Bogorad RL, Sancak Y, Kamer KJ, Strittmatter L, Li AA, Girgis HS, Kuchimanchi S, De Groot J, Speciner L, et al. (2013). MICU2, a paralog of MICU1, resides within the mitochondrial uniporter complex to regulate calcium handling. PLoS ONE 8, e55785. [PubMed: 23409044]

Raffaello A, De Stefani D, Sabbadin D, Teardo E, Merli G, Picard A, Checchetto V, Moro S, Szabó I, and Rizzuto R (2013). The mitochondrial calcium uniporter is a multimer that can include a dominant-negative poreforming subunit. EMBO J. 32, 2362–2376. [PubMed: 23900286]

Rayavarapu S, Coley W, Cakir E, Jahnke V, Takeda S, Aoki Y, Grodish-Dressman H, Jaiswal JK, Hoffman EP, Brown KJ, et al. (2013). Identification of disease specific pathways using in vivo SILAC proteomics in dystrophin deficient mdx mouse. Mol. Cell. Proteomics 12, 1061–1073. [PubMed: 23297347]

Rudolf R, Mongillo M, Magalhães PJ, and Pozzan T (2004). In vivo monitoring of Ca(2+) uptake into mitochondria of mouse skeletal muscle during contraction. J. Cell Biol 166, 527–536. [PubMed: 15314066]

Sancak Y, Markhard AL, Kitami T, Kovács-Bogdán E, Kamer KJ, Udeshi ND, Carr SA, Chaudhuri D, Clapham DE, Li AA, et al. (2013). EMRE is an essential component of the mitochondrial calcium uniporter complex. Science 342, 1379–1382. [PubMed: 24231807]

Seifert EL, Bézaire V, Estey C, and Harper ME (2008). Essential role for uncoupling protein-3 in mitochondrial adaptation to fasting but not in fatty acid oxidation or fatty acid anion export. J. Biol. Chem 283, 25124–25131. [PubMed: 18628202]

Shamseldin HE, Alasmari A, Salih MA, Samman MM, Mian SA, Alshidi T, Ibrahim N, Hashem M, Faqeih E, Al-Mohanna F, and Alkuraya FS (2017). A null mutation in MICU2 causes abnormal

mitochondrial calcium homeostasis and a severe neurodevelopmental disorder. Brain 740, 2806–2813.

Spurney CF, Gordish-Dressman H, Guerron AD, Sali A, Pandey GS, Rawat R, Van Der Meulen JH, Cha HJ, Pistilli EE, Partridge TA, et al. (2009). Preclinical drug trials in the mdx mouse: assessment of reliable and sensitive outcome measures. Muscle Nerve 30, 591–602.

Tiepolo T, Angelin A, Palma E, Sabatelli P, Merlini L, Nicolosi L, Finetti F, Braghetta P, Vuagniaux G, Dumont JM, et al. (2009). The cyclophilin inhibitor Debio 025 normalizes mitochondrial function, muscle apoptosis and ultrastructural defects in Col6a1−/− myopathic mice. Br. J. Pharmacol 157, 1045–1052. [PubMed: 19519726]

Tsai CW, Wu Y, Pao PC, Phillips CB, Williams C, Miller C, Ranaghan M, and Tsai MF (2017). Proteolytic control of the mitochondrial calcium uniporter complex. Proc. Natl. Acad. Sci. USA 114, 4388–4393. [PubMed: 28396416]

Vecellio Reane D, Vallese F, Checchetto V, Acquasaliente L, Butera G, De Filippis V, Szabó I, Zanotti G, Rizzuto R, and Raffaello A (2016). A MICU1 Splice Variant Confers High Sensitivity to the Mitochondrial Ca^{2+} Uptake Machinery of Skeletal Muscle. Mol. Cell 64, 760–773. [PubMed: 27818145]

Vila MC, Rayavarapu S, Hogarth MW, Van der Meulen JH, Horn A, Defour A, Takeda S, Brown KJ, Hathout Y, Nagaraju K, and Jaiswal JK (2017). Mitochondria mediate cell membrane repair and contribute to Duchenne muscular dystrophy. Cell Death Differ. 24, 330–342. [PubMed: 27834955]

Wang L, Yang X, Li S, Wang Z, Liu Y, Feng J, Zhu Y, and Shen Y (2014). Structural and mechanistic insights into MICU1 regulation of mitochondrial calcium uptake. EMBO J. 33, 594–604. [PubMed: 24514027]

Yang T, Ta TA, Pessah IN, and Allen PD (2003). Functional defects in six ryanodine receptor isoform-1 (RyR1) mutations associated with malignant hyperthermia and their impact on skeletal excitation-contraction coupling. J. Biol. Chem 278, 25722–25730. [PubMed: 12732639]

Zampieri S, Mammucari C, Romanello V, Barberi L, Pietrangelo L, Fusella A, Mosole S, Gherardi G, Höfer C, Löfler S, et al. (2016). Physical exercise in aging human skeletal muscle increases mitochondrial calcium uniporter expression levels and affects mitochondria dynamics. Physiol. Rep 4, e13005. [PubMed: 28039397]

Highlights

- MICU1 is central to coupling MCU to skeletal muscle excitation and contraction
- Muscle-specific lack of MICU1 in mouse recaps skeletal muscle symptoms in patients
- Loss of the bioenergetic role of MICU1 contributes to muscle weakness and fatigue
- Impaired membrane repair contributes to myofiber damage and high serum CK levels

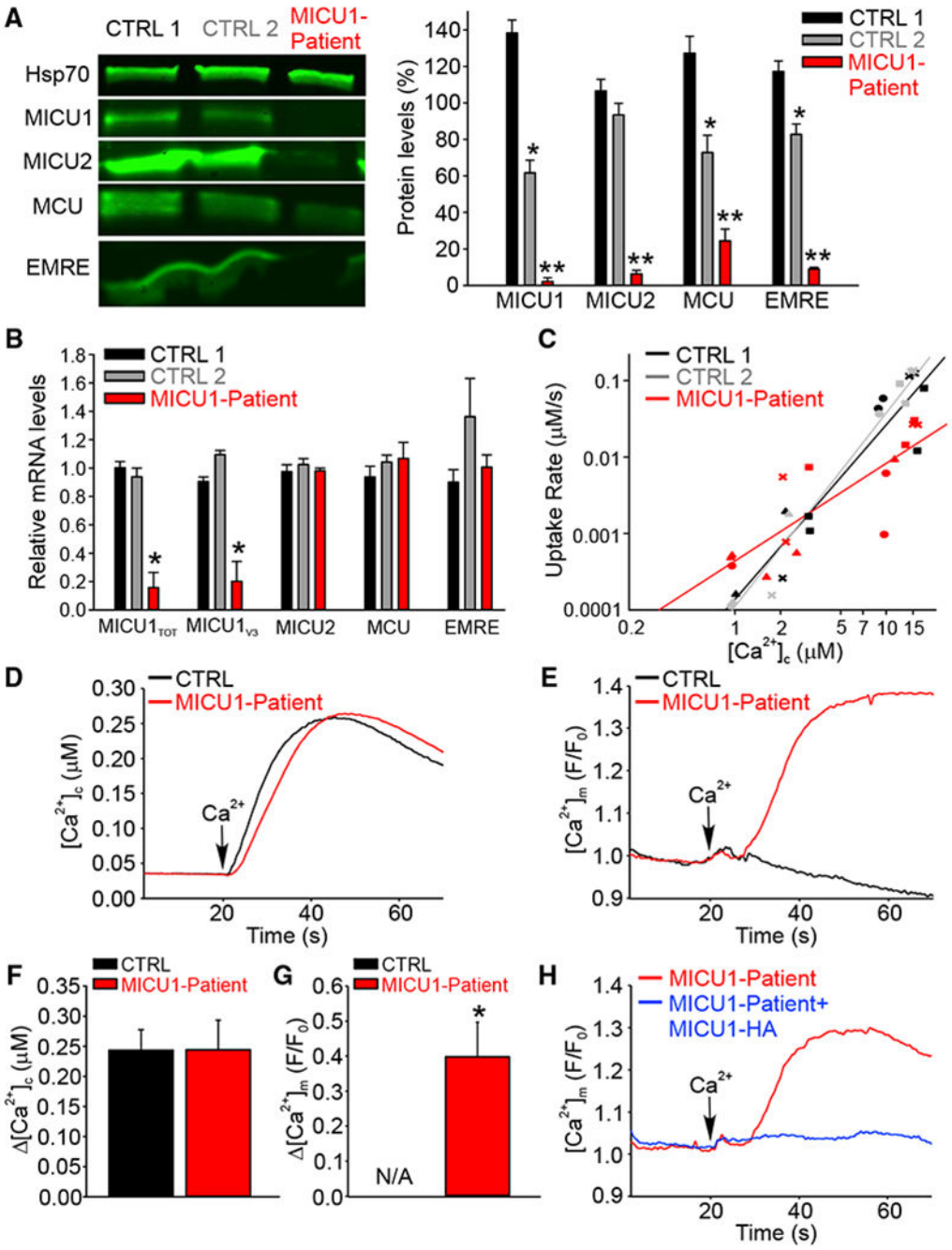

Figure 1. MCU Complex Composition and Mitochondrial Ca^{2+} Handling in Fibroblasts from MICU1 Loss-of-Function Patients

(A) Representative immunoblots of Hsp70, MICU1, MICU2, MCU, and EMRE in control (CTRL; CTRL1 and CTRL2) and MICU1-patient fibroblasts. Relative protein levels are displayed in the bar graph; each protein was normalized to Hsp70, and expressed relative to the mean of CTRL1 and CTRL2 fibroblasts (n = 3, *p < 0.05, **p < 0.01).

(B) Relative mRNA levels of total MICU1 ($MICU1_{TOT}$), transcript variant 3 of MICU1 ($MICU1_{v3}$), MICU2, MCU, and EMRE. Each transcript was normalized to β-actin mRNA, and expressed relative to the mean of CTRL1 and CTRL2 fibroblasts (n = 3, *p < 0.05).

Double-logarithmic plot of the initial rates of Ca^{2+} uptake against the peak free $[Ca^{2+}]_c$. Slope of each linear fit is indicated. The following total $CaCl_2$ additions were applied: 3, 4, 5, 6, 10, and 30 μM (mean ± SEM, n = 4). For calculation of the initial rates linear fits were used because exponentials could not be fit well when the uptake was small. However, the exponential fit is expected to be different from the linear fit when the Ca^{2+} clearance is substantial, so we recalculated the uptake rates at $[Ca^{2+}]_c$ of 15 μM, where the CTRLs gave 0.116 ± 0.0176 μM/s and the MICU1-patient showed 0.026 ± 0.0038 μM/s ($p < 0.05$, Mann-Whitney), confirming a decrease in the mitochondrial Ca^{2+} uptake in the MICU1-patient at > 10 μM $[Ca^{2+}]_c$.

(D and E) Mean time courses from SOCE-associated $[Ca^{2+}]_c$ (fura2) (D) and $[Ca^{2+}]_m$ (mtCepia) (E) signals monitored separately in fibroblasts pretreated with Tg in a Ca^{2+}-free ECM. To evoke SOCE, 1.5 mM $CaCl_2$ (Ca^{2+}) was added (n = 12 cells for each).

(F and G) SOCE-associated $[Ca^{2+}]_c$ and $[Ca^{2+}]_m$ response expressed as difference between peak and baseline ($\Delta[Ca^{2+}]_c$ in [F] and $\Delta[Ca^{2+}]_m$ in [G]). Experiments were as in (D) and (E), respectively.

(H) Mean traces of the $[Ca^{2+}]_m$ responses to SOCE in MICU1-patient and MICU1-HA-rescued human fibroblasts (n = 22–24 cells for each).

In all cases, values represent the mean ± SEM.

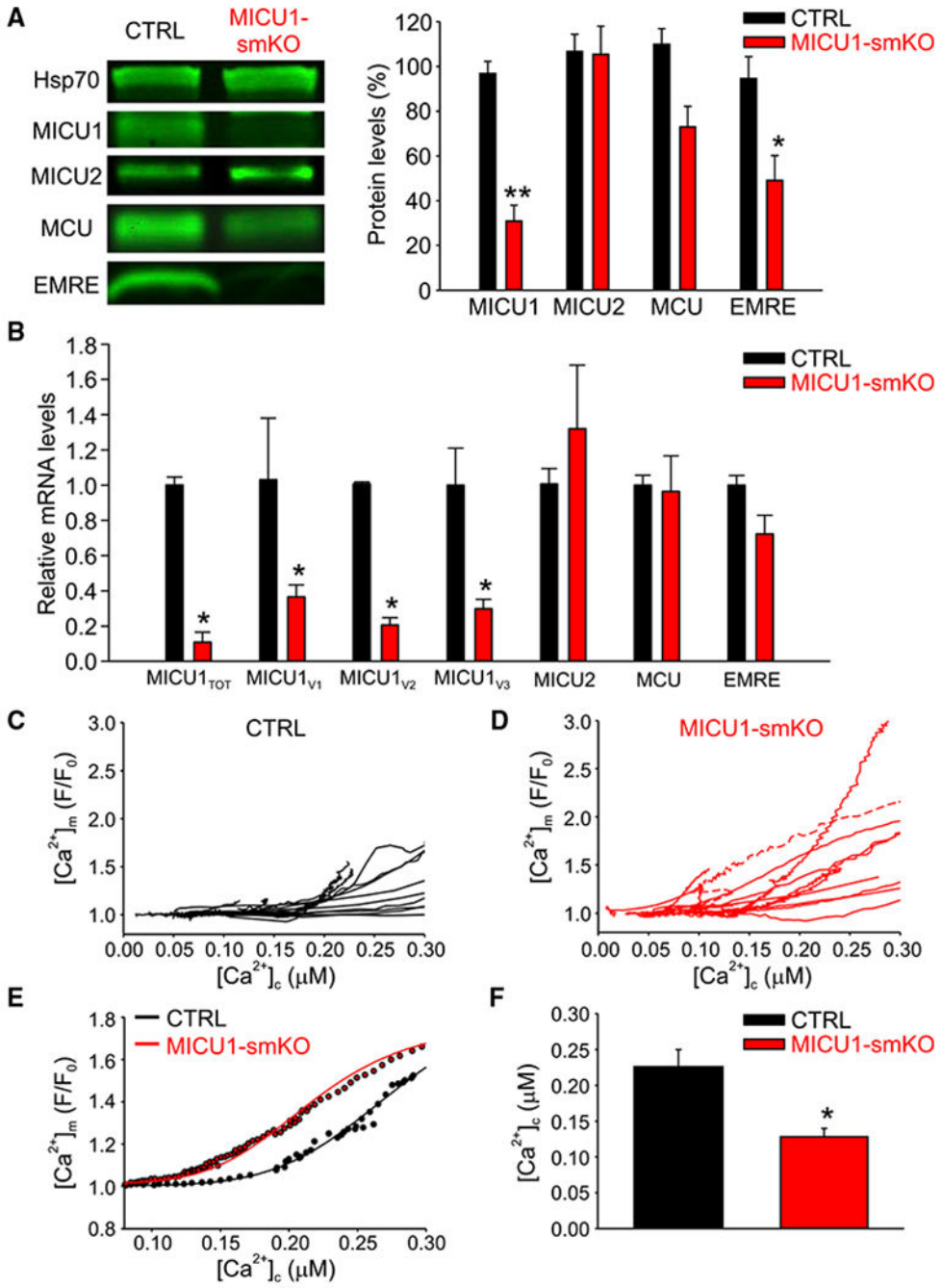

Figure 2. Ablation of MICU1 in Mouse SM

(A) Representative immunoblots of Hsp70, MICU1, MICU2, MCU, and EMRE in SM from CTRL Micu1$^{F/F}$ (CTRL, black bars) and muscle-specific (CK promoter-drive Cre recombinase) MICU1 knockout (MICU1-smKO, red bars) mice. Relative protein levels are displayed in the bar graph; each proteinwas normalized to Hsp70, and expressed relative to CTRL (mean ± SEM, n = 3, *p < 0.01, **p < 0.001).

Relative mRNA levels of total MICU1 (MICU1tot), transcript variant 3 of MICU1 ($MICU1_{v3}$), transcript variant 2 of MICU1 ($MICU1_{v2}$; also known as MICU1.1), transcript

variant 1 of MICU1 ($MICU1_{v1}$), MICU2, MCU, and EMRE in SM from CTRL and MICU1-smKO mice. Each transcript was normalized to β-actin mRNA and expressed relative to CTRL (mean ± SEM, n = 3, *$p < 0.05$, Student's t test).

(C and D) $[Ca^{2+}]_m$ (mtRCaMP) versus $[Ca^{2+}]_c$ (fura2) curves from individual CTRL (C) and MICU1-smKO (D) isolated SM fibers. Fibers were pretreated with Tg in a Ca^{2+}-free ECM. To evoke SOCE, 2 mM $CaCl_2$ (Ca^{2+}) was added (n = 15–16 fibers).

(E) Mean traces of the $[Ca^{2+}]_m$ responses versus SOCE-associated $[Ca^{(2)}_c$ for CTRL and MICU1-smKO from (D) and (E), respectively.

$[Ca^{2+}]_c$ at which CTRL and MICU1-smKO fibers showed a 10% increase in $[Ca^{2+}]_m$ (expressed as F/F_0 of mtRCaMP). Experiments were as in (C) and (D).

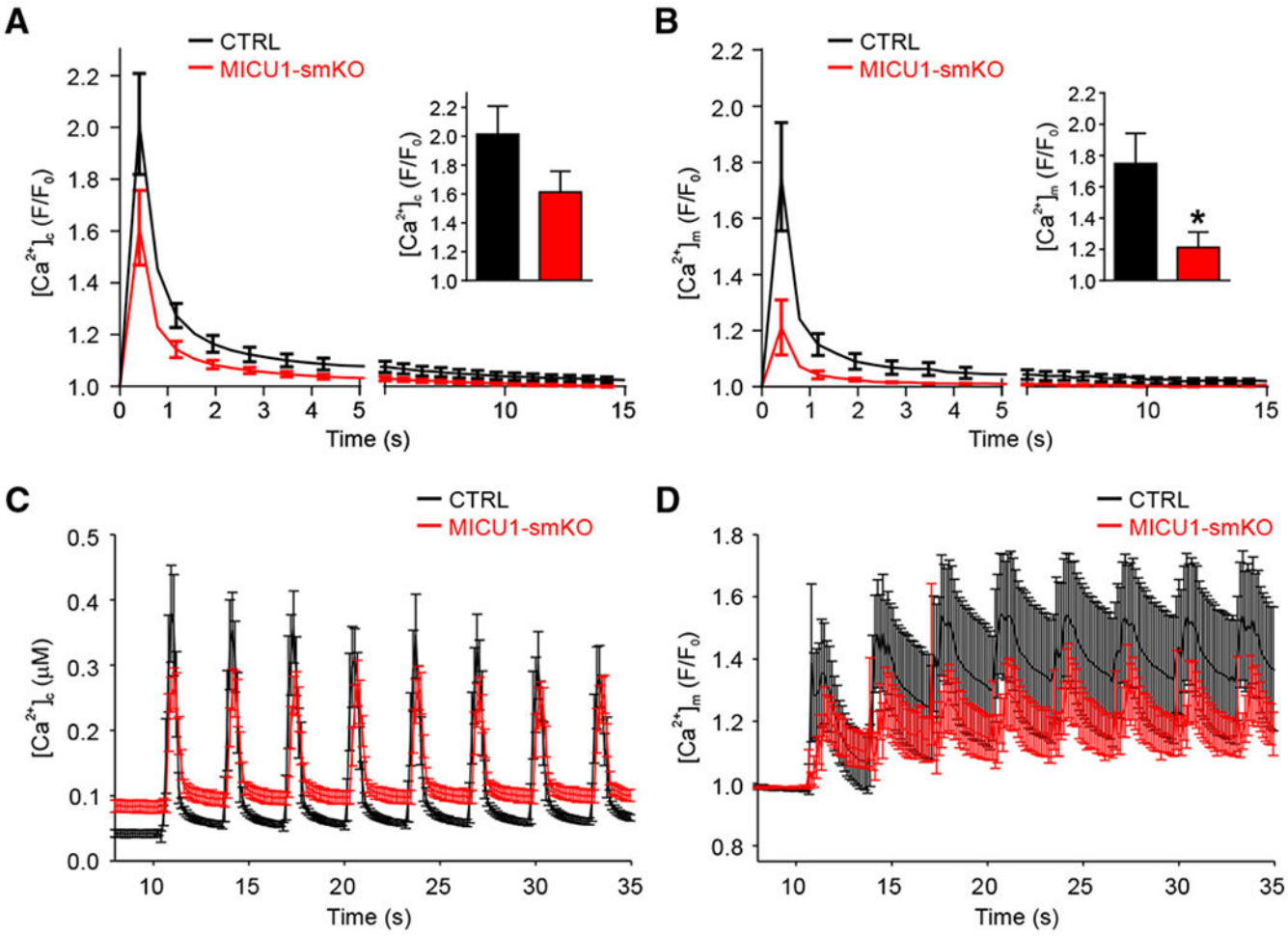

Figure 3. MICU1 Is Required for Normal Ca^{2+} Transients during SM Contraction

(A and B) Plots showing Ca^{2+} changes following twitch stimulation of FDB myofibers from CTRL and MICU1-smKO mice (100-ms pulse of 20V). Each fiber received five twitch stimulations (60 s apart) and these responses were averaged to obtain a single averaged trace for that fiber (n = 10 CTRL and 14 MICU1-smKO fibers each).

(A) Averaged trace of Fluo-4 intensity after twitch stimulation. Insert shows peak $[Ca^{2+}]_c$.

(B) Averaged trace showing Rhod-2 intensity after twitch stimulation. Insert shows peak $[Ca^{2+}]_m$. Asterisk indicates $p < 0.05$ by Mann-Whitney test. (C and D) Repetitive tetanic stimulation of FDB fibers (2-ms pulse at 65 Hz, for 500 ms every 2.5 s) from CTRL and MICU1-smKO: cytosolic and mitochondrial Ca^{2+} results were measured upon transfection with mtRCaMP, mtYFP (to normalize for contractile movements), and loading with Fura-2 AM.

(C) Initial cytosolic Ca^{2+} transients during 100 tetani ES (n = 14, 12).

(D) Initial mitochondrial Ca^{2+} transients during 100 tetani ES (n = 9).

In all panels, values are the mean ± SEM.

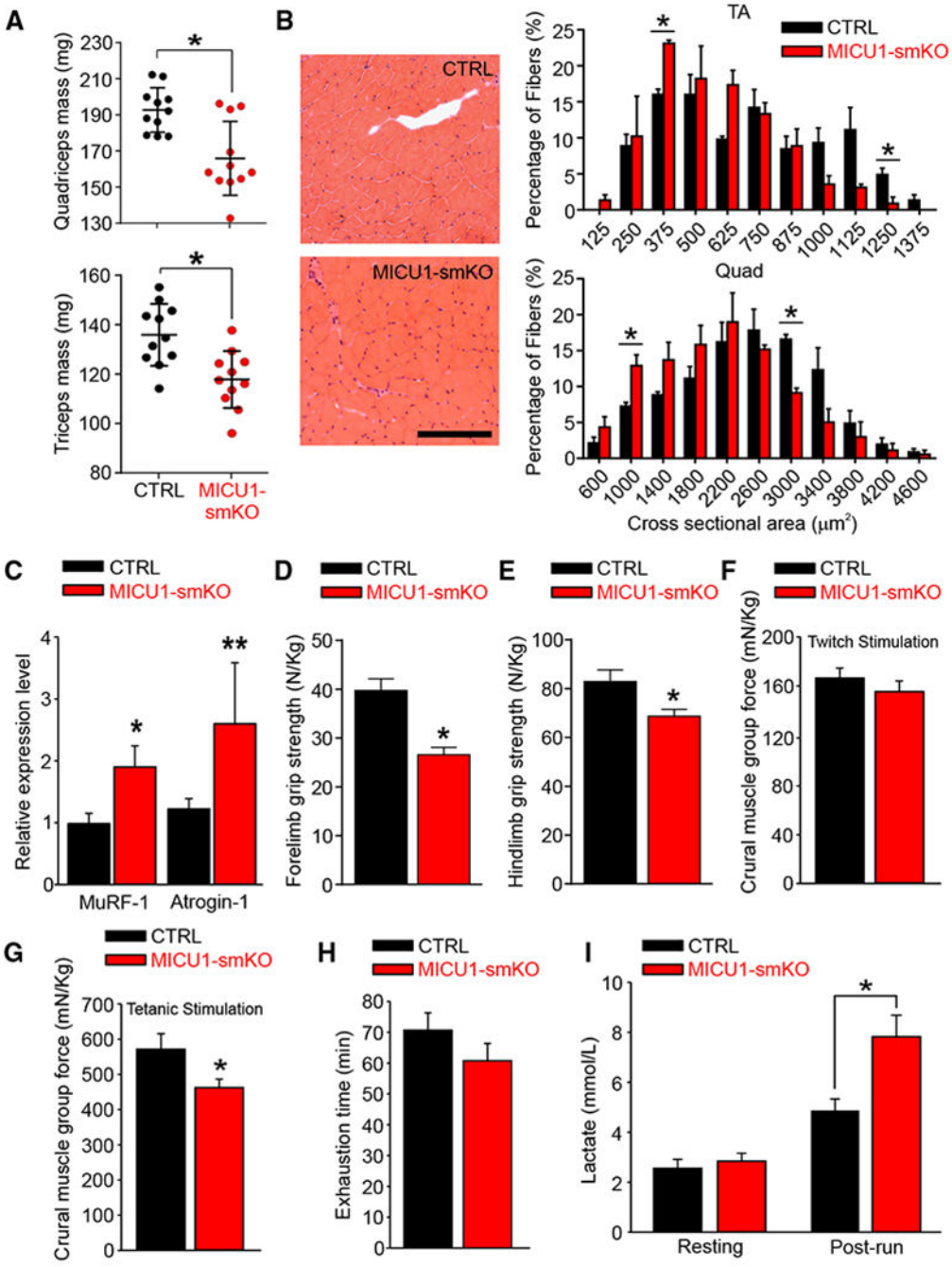

Figure 4. Lack of MICU1 Causes Muscle Atrophy and Decreased Strength

(A) Plot showing quadriceps and triceps muscle mass; each dot represents one muscle (*p < 0.05).

(B) Cross sections from TA stained with H&E to evaluate fiber cross-sectional areas (left; scale bar, 100 μm). Distribution of the cross-sectional areas in TA and quadriceps (right; > 100 fibers per muscle; n = 3 mice/genotype).

(C) Relative mRNA levels of Murf-1 and Atrogin-1. Each transcript was normalized to β-actin mRNA, and expressed relative to CTRL (n = 6/genotype, *p < 0.01, **p < 0.05).

(D and E) Averaged forelimb (D) and hindlimb (E) grip strength measurement (n = 6 mice each; *p < 0.05).
(F and G) Maximal force developed during (F) twitch and (G) tetanic stimulation of anterior crural muscle group (n = 10 muscles/genotype; *p < 0.05).
(H) Treadmill running time during exhaustion protocol (n = 8).
(I) Blood levels of lactate at rest (n = 14–16) and after running exhaustion protocol on the treadmill (n = 8, *p < 0.002).
All bar charts show the mean ± SEM.

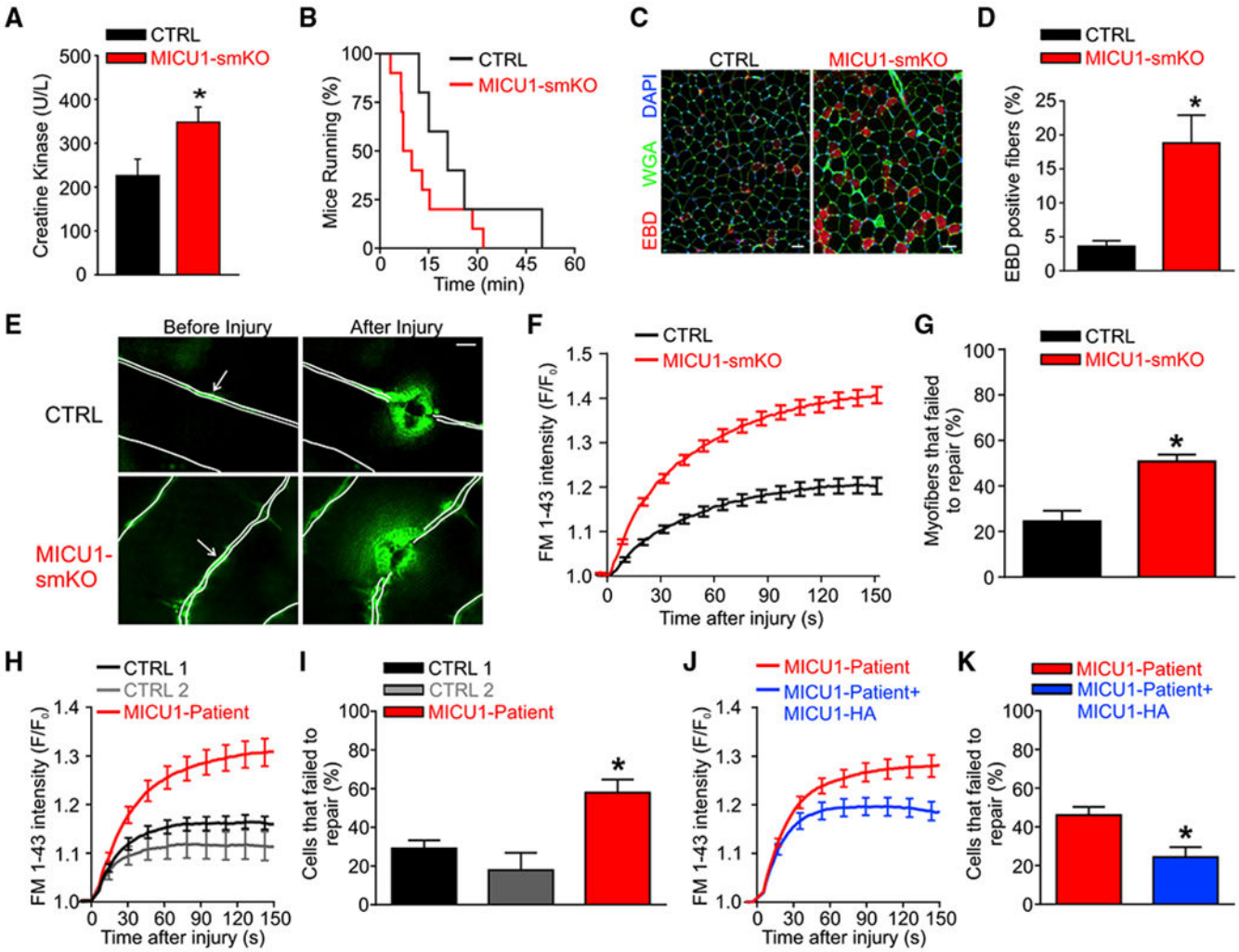

Figure 5. Mouse Myofibers and Patient Fibroblasts Lacking MICU1 Show Poor Plasma Membrane Repair

(A-G) Data from mice.

(A) Serum levels of CK (n = 12 CTRL and 15 MICU1-smKO; *p < 0.02).

(B) Plot showing length of time mice ran voluntarily on a flat treadmill 24 h after eccentric exercise (n = 5 CTRL, 10 MICU1-smKO).

(C and D) Images (scale bar, 50 μm) (C) and quantification (D) of Evan's blue dye (EBD) uptake in the quadriceps of mice 24 h after eccentric exercise. Wheat germ albumin (WGA) marks the boundary of individual myofibers (n = 10 CTRL, 8 MICU1-smKO muscles; *p < 0.05).

(E-G) Images (scale bar, 10 μm) (E), kinetics of FM1-43 dye uptake in myofibers after focal laser injury (n = 60 CTRL, 118 MICU1-smKO myofibers) (F), and quantification of myofibers that failed to repair after laser injury (G). Solid line in (E) marks the boundary of individual myofibers (n = 6 independent experiments; *p < 0.05).

(H-K) Data from patient fibroblasts.

(H) Plot showing kinetics of FM1-43 dye uptake after focal laser injury in CTRL and MICU1-patient fibroblasts (n = 20 CTRL1, 16 CTRL2, 46 MICU1-patient fibroblasts).

(I) Quantification of fibroblasts that failed to repair 4 min post focal laser injury (n = 3 independent experiments; *p < 0.05).
(J) Plot showing kinetics of FM1-43 dye uptake after focal laser injury in CTRL-transfected or MICU1-HA-transfected patient fibroblasts (n = 36 MICU1-patient, 32 Patient+MICU1-HA fibroblasts).
(K) Quantification of fibroblasts that failed to repair from focal laser injury (n = 4 independent experiments; *p < 0.05).
All values: mean ± SEM.

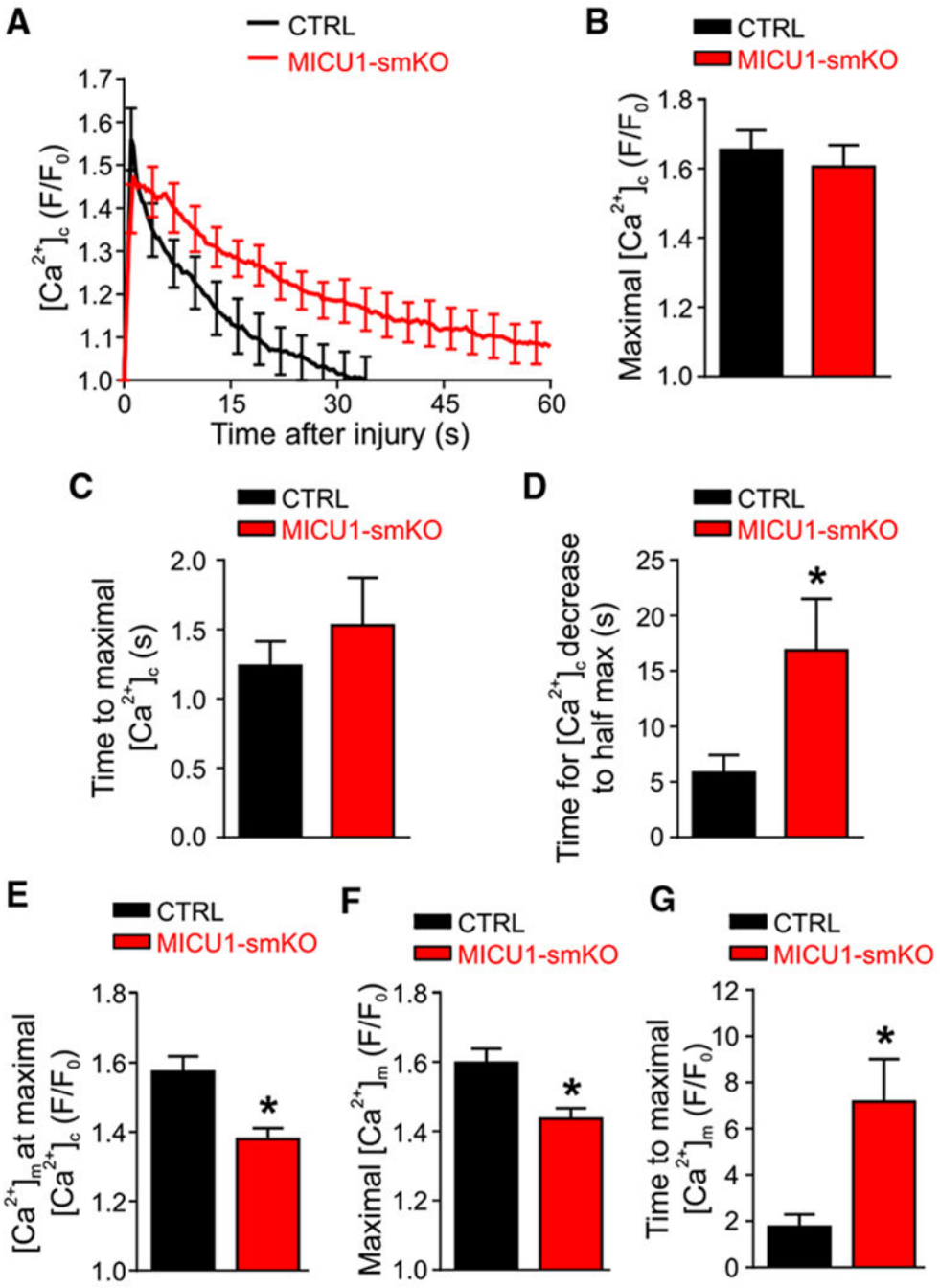

Figure 6. Lack of MICU1 Alters Cytosolic and Mitochondrial Ca^{2+} Kinetics following Myofiber Sarcolemma Injury

(A) Plot showing the kinetics of change in cytosolic calcium (measured by fluo-4) after focal sarcolemmal laser injury.

(B–D) Quantification of data in (A) showing (B) peak $[Ca^{2+}]_c$, (C) time for $[Ca^{2+}]_c$ to reach the peak, and (D) time for $[Ca^{2+}]_c$ to decrease from peak to half-peak after laser injury.

(E) $[Ca^{2+}]_m$ quantified for each myofiber when its $[Ca^{2+}]_c$ was at its peak.

(F) Peak $[Ca^{2+}]_m$ after focal laser injury.

(G) Plot showing time to peak $[Ca^{2+}]_m$ after focal laser injury. In all cases, n = 13 CTRL and 15 MICU1-smKO myofibers, *$p < 0.05$.
Values are the mean ± SEM.

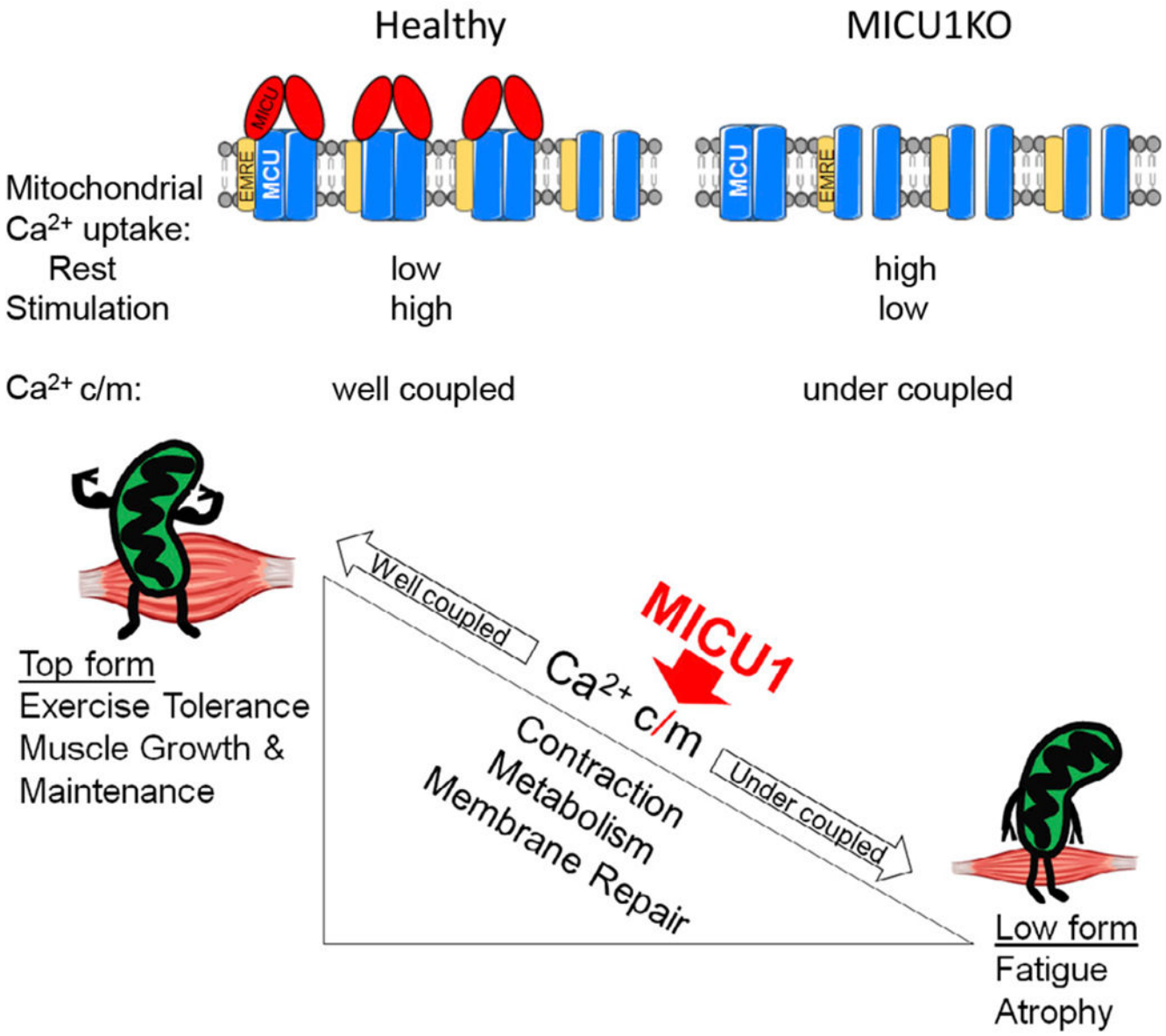

Figure 7. Loss of MICU1 Changes the Functional Coupling between Cytosolic and Mitochondrial Ca^{2+} Leading to Lower Fitness of SM

Our study focused on outcomes of SM health in response to resting and stimulated Ca^{2+} regimes, in the presence and absence of mtCU regulation by MICU1. Preventing uniporter regulation led to higher resting $[Ca^{2+}]_m$ and less mitochondrial Ca^{2+} uptake during stimulation. The changed mitochondrial Ca^{2+} phenotypes in response to cytosolic Ca^{2+} regimes were associated with lower exercise capacity and muscle mass. We therefore hypothesize that the functional coupling between cytosolic and mitochondrial Ca^{2+} (Ca^{2+} c/m) contributes to the fitness of SM, and that the regulation of mtCU is an effector of this coupling. We further propose that contractile performance, metabolism, and membrane repair are mechanisms that link MICU1 regulation of mtCU to exercise performance and SM mass. Also represented is the lower EMRE expression with MICU1 depletion, leading to some nonfunctional mtCUs that would protect against mitochondrial Ca^{2+} overload. The

lower EMRE expression with MICU1 loss also suggests that another role for MICU1 is to contribute to the stability of the mtCU complex.

KEY RESOURCES TABLE

REAGENT or RESOURCE	SOURCE	IDENTIFIER
Antibodies		
Rabbit anti-MICU1	Sigma Aldrich	Cat#HPA036480
Rabbit anti-MICU2	Abcam	Cat#ab101465
Rabbit anti-MCU	Sigma Aldrich	Cat#HPA016480; RRID: AB_2071893
Rabbit anti-EMRE	Santa Cruz	Cat#sc86336 (discontinued)
Mouse anti-Hsp60	Thermo Scientific	Cat#MA3-028
Rabbit anti-phospho-AKT (Ser473)	Cell Signaling Technology	Cat#9271
Rabbit anti-AKT	Cell Signaling Technology	Cat#9272; RRID: AB_329827
Rabbit anti-phospho-AMPKα (Thr172)	Cell Signaling Technology	Cat#2535
Rabbit anti-AMPKα	Cell Signaling Technology	Cat#2532
Rabbit anti-phospho-S6 (ser235/236)	Cell Signaling Technology	Cat#2211; RRID: AB_331679
Rabbit anti-S6 Ribosomal Protein	Cell Signaling Technology	Cat#2217; RRID: AB_331355
Mouse Total-OxPhos Cocktail	Abcam	Cat#ab110411; RRID: AB_2756818
Goat Anti-GRB2	Abcam	Cat#ab2234; RRID: AB_2113027
Rabbit anti-laminin	Sigma Aldrich	Cat#L9393; RRID: AB_477163
Mouse anti-myosin heavy chain Type I	Developmental Studies Hybridoma Bank	Cat#BA-D5; RRID: AB_2235587
Mouse anti-myosin heavy chain Type2A	Developmental Studies Hybridoma Bank	Cat#SC-61
Mouse anti-myosin heavy chain Type2B	Developmental Studies Hybridoma Bank	Cat#BF-F3; RRID: AB_2266724
Chicken anti-rabbit Alexa Fluor488 conjugated to Dylight 488	Invitrogen	Cat#A21441; RRID: AB_141735
Goat anti-mouse Alexa Fluor647 conjugated to Dylight 405	Invitrogen	Cat#21235; RRID: AB_141693
Chemicals, Peptides, and Recombinant Proteins		
DC™ Protein Assay	BioRad	Cat#5000112
Lipofectamine 3000	Invitrogen	Cat#L3000015
Hyaluronidase Type IV	Sigma Aldrich	Cat#H4272
Collagenase Type 2	Thermo Fisher	Cat#16101015
Matrigel	BD Biosciences	Cat#356234
TRIzol Reagent	Ambion	Cat#15596018
SuperScript III	Invitrogen	Cat#18080085
Thapsigargin	Enzo Life Sciences	Cat#BML-PE180
CGP-37157	Enzo Life Sciences	Cat#BML-CM119
Fura2 AM/salt	Teflabs	Cat# 0-103/0-104
Fura-lowAff AM/salt	Teflabs	Cat# 0-136/0-0137
Fluo4/AM	Invitrogen	Cat# F14201
Prolong Gold Mounting Media	Life Technologies	Cat#P10144
FM1-43 dye	Life Technologies	Cat#T3163

REAGENT or RESOURCE	SOURCE	IDENTIFIER
Critical Commercial Assays		
Animal Tissue RNA Purification Kit	Norgen Biotek	Cat#25700
Enzy Chrome Creatine Kinase Assay Kit	BioAssay Systems	Cat#ECPK-100
Experimental Models: Cell Lines		
Human fibroblasts (Control and *MICU1* variant)	PMID: 27123478	Patient “IV:6” in PMID: 27123478
Experimental Models: Organisms/Strains		
Mouse: MICU1 floxed ($MICU1^{F/F}$)	PMID: 26956930	N/A
Mouse: Ckmm-Cre-$MICU1^{F/F}$ (MICU1-smKO)	This paper	N/A
Mouse: Tg(Ckmm-Cre)	Jackson Laboratories	JAX stock# 006475
Oligonucleotides		
Genotyping primer (MICU1F/F)FWD GGT GGA GTC AAA GGG AGG AAC AG	This paper	N/A
Genotyping primer (MICU1F/F) REV GCC CCA TCT ATG ATA ATG TTA AGC	This paper	N/A
Genotyping primer (MICU1-smKO) FWD CAG AAC CTG AAG ATG TTC GC	This paper	N/A
Genotyping primer (MICU1-smKO) REV TAC ACC TCG GTG CTA ACC AG	This paper	N/A
qPCR Primers listed in Table S1	This paper	N/A
Recombinant DNA		
pCMV Cepia3mt	PMID: 24923787	Addgene#58219
mtRCaMP	PMID: 22784666	N/A
pEYFP-mito	Clontech	6115-1
Software and Algorithms		
SigmaPlot	Systat Software	N/A
GraphPad Prism	Scientific Software	N/A
Slidebook 6.0 Image Acquisition Software	Intelligent Imaging Innovations Inc.	N/A
CellSens 1.13	Olympus	N/A
VS-ASW FL 2.7 Imaging Software	Olympus	N/A
Other		
In situ Muscle Test System 1300A	Aurora Scientific	N/A
Rodent Treadmill Exer 3/6	Columbus Instruments	1055-SRM
Grip Strength Meter	Columbus Instruments	1027SM
Lactate Plus Meter	Nova Biomedical	N/A
Cryostat CM1900	Leica	N/A
Square Pulse Stimulator SD9	Grass Technologies	N/A
Oscilloscope NDS-220	Tektronix	N/A
Culture/Stimulation Chamber	Cell MicroControls	N/A
Multiwavelength excitation dual wavelength emission fluorimeter	Horiba/PTI	N/A
Ablate! Pulse Laser	3i Intelligent Imaging Innovations	N/A

REAGENT or RESOURCE	SOURCE	IDENTIFIER
Zeiss LSM 780 Confocal laser-scanning microscope	Carl Zeiss	N/A
Zeiss Axio Observer Microscope	Carl Zeiss	N/A
Leica Inverted DMRE Epi-Fluorescence Microscope	Leica	N/A
Olympus 1X70 Inverted Fluorescence Microscope	Olympus	N/A
Olympus BX61 Inverted Fluorescence Microscope	Olympus	N/A
Olympus 1X81 Inverted Fluorescence Microscope	Olympus	N/A
CSU-XI Spinning Disc Confocal Unit	Yokogawa Electric Co.	N/A
Tokai Hit Microscope with ZILCS Incubator	Tokai Hit Co.	N/A
DFC420 Digital Camera	Leica	N/A
Evolve 512 EMCCD Camera	Photometrics	N/A
Olympus XM10 Monochrome Camera	Olympus	N/A
ProEM 1024 EMCCD Camera	Princeton Instruments	N/A